12-2017

Numerical Simulations of Turbulent Pulsed Jet Flame

Jie Tao
Purdue University

Recommended Citation

Tao, Jie, "Numerical Simulations of Turbulent Pulsed Jet Flame" (2017). *Open Access Theses*. 1325.
https://docs.lib.purdue.edu/open_access_theses/1325

NUMERICAL SIMULATIONS OF TURBULENT PULSED JET FLAME

A Thesis

Submitted to the Faculty

of

Purdue University

by

Jie Tao

In Partial Fulfillment of the

Requirements for the Degree

of

Master of Science in Aeronautical and Astronautical Engineering

December 2017

Purdue University

West Lafayette, Indiana

THE PURDUE UNIVERSITY GRADUATE SCHOOL
STATEMENT OF THESIS APPROVAL

Dr. Haifeng Wang, Chair
    School of Aeronautics and Astronautics
Dr. Gregory A. Blaisdell
    School of Aeronautics and Astronautics
Dr. Terrence R. Meyer
    School of Mechanical Engineering

Approved by:
    Dr. Weinong Wayne Chen
        Aeronautics and Astronautics Associate Head for Graduate Education

ACKNOWLEDGMENTS

Firstly, I would like to express my highest appreciation to my advisor, Professor Haifeng Wang, for offering me the great opportunity to work with him for the past two years. His patience, professional guidance and persistent help have led me through this thesis study and inspired me to practice critical thinking. And then, I also would like to express my gratefulness to Professor Gregory A. Blaisdell and Professor Terrence R. Meyer for being on my committee. Their courses in aerodynamics, fluid mechanics, turbulence and combustion have introduced a novel world to me.

Secondly, I am deeply thankful to all members in Computational Energy and Propulsion Laboratory at Purdue, Ms. Pei Zhang, Mr. Chao Han, Mr. Tejas A. Pant, Mr. Tianfang Xie, Mr. Utsav Jain, Mr. Menglin Ni, Mr. Shashank S. Kashyap, Mr. Xiao Jing, Dr. Harshad Lalit, and Mr. Akshay Koodly-Ravishankara for their assistance whenever I have encountered a problem.

Thirdly, I am forever indebted to my parents whom sacrifice themselves to support me and for making me who I am.

Finally, thank you my beloved wife Ho-An Chien for the unconditional love.

TABLE OF CONTENTS

LIST OF TABLES

LIST OF FIGURES

Figure Page

SYMBOLS

f	probability density function
k	turbulent kinetic energy
s_0	origin of scaled time
t	time
u	velocity
w	particle wieght
x	physical axis
C_ϕ	mixing coefficient
N_{pc}	particle number in a cell
P_k	production of turbulent kinetic energy
U, V, W	velocity
W	edge weight
δ_{ij}	Kronecker delta
ϵ	dissipation
μ	dynamic viscosity
μ_t	turbulent viscosity
ξ	fuel mixture fraction
ρ	density
ϕ	composition vector
ω	turbulent coefficient
Ψ	composition space

ABBREVIATIONS

CFD	Computational Fluid Dynamics
CNG	Compressed Natural Gas
EMST	Euclidean Minimum Spanning Tree
GRI	Gas Research Institute
IEM	Interaction by Exchange with the Mean
ISAT	In Situ Adaptive Tabulation
LES	Large Eddy Simulation
PDF	Probability Density Function
RANS	Reynold Averaged Navier-Stokes

ABSTRACT

Tao, Jie M.S., Purdue University, December 2017. Numerical simulations of turbulent pulsed jet flame. Major Professor: Dr. Haifeng Wang.

In this study, computational fluid dynamics (CFD) calculations for a turbulent pulsed jet flame are performed coupling Reynolds Average Navier-Stokes (RANS) $k-\epsilon$ model, Probability Density Function (PDF) with particle method and a 19-species reduced GRI chemistry reaction mechanism. In the first part of this study, a base flame of the turbulent pulsed jet flame, Sydney Flame L, is simulated for parametric studies to obtain optimal numerical and modeling settings, and these settings can be used in the turbulent pulsed jet flame to perform simulations accurately. The effect of mixing models and mixing parameter is emphasized in the parametric study since they have significant effect on the predicted extinction limit. In the second part of this study, comprehensive RANS/PDF simulations of turbulent pulsed jet flame are performed. The extinction gap, observed in experiment is reproduced by two out of three mixing models, with the extinction gap sensitive to mixing coefficient. Gap location history and velocity history are compared with experimental data at multiple selected locations. Good agreement has been achieved for the velocity field while the extinction gap show some deviation from experiment.

1. INTRODUCTION

1.1 Background

Oil, natural gas and coal took up about 85 percent of the world energy consumption in 2016 with percentage of natural gas keeping increasing in the past years [1]. Fossil fuels remain the most important energy source to human beings. Since combustion is the major solution to transfer chemical energy from the three mentioned fuels into usable energy for human being. Increasing combustion efficiency remains as one of the top priorities in combustor design. Having a clear understanding of combustion process leads to better utilization of fossil fuels.

Through years, researchers use various models to investigate all kinds of combustion problems and flames, like gas turbine. Most research studies focused on simulating steady/statistical stationary flames for developing/validating combustion models, like multiple flames that discussed in TNF workshop [2]. But few research studies focused on statistical transient flame. Transient combustion dynamics are critically important to the design of robust combustors. Highly complicated transient combustion dynamics occurs in various scenarios such as reciprocating piston engine, gas turbine starting. Thus it is imperative to have a good understanding in the transient combustion dynamics.

Since almost all combustion applications are related to turbulence and combustion, combination of these two subjects dramatically increases the difficulty of solving this problem. Turbulence itself, as one of the unsolved classical physics problems, has already been studied by researchers all around the world for more than a hundred of years. Yet it is still unknown how to describe turbulence exactly using a theoretical model. Several families of models have been developed based on different levels of details they contain. Direct Numerical Simulation (DNS) [3] [4] is developed to solve the Navier-Stokes equation with resolutions of space and time both to Kolmogorov scale. Since all scales larger than Kolmogorov scale are solved, tremendous computational resource is required. Thus, only low Reynolds number or relatively small computational domain are possible to implement DNS method.

If a certain level of scale is of interest in the flow field, then solving all larger scale and modeling smaller scale can help to study this flow field. Based on the above demand, Large Eddy Simulation (LES) [5] comes into play. Where LES adopts low-pass filter to filter out high frequency fluctuations that related to smaller scale and are usually computationally expensive. Base on the increasing of computational power nowadays, LES is much more feasible to practice in engineering problems.

Reynolds Averaged Navier-Stoke (RANS) is widely used in industries in the past twenties years. Since it only solves mean flow field with all fluctuation modeled, it requires less computational resource and is efficient to generate an answer. Multiple models has been developed for RANS method: standard $k-\epsilon$ model [6], Wilcox $k-\omega$ model [7], etc.

As for combustion, extensive efforts have been put into developing models to predict combustion processes accurately, including: ignition, extinction, sooting etc. Many combustion models have been developed: flamelet model, Linear Eddy Model (LEM), Conditional Moment Closure (CMC), Probability Density Function (PDF) model etc. Among those combustion models, Probability Density Function (PDF) model [8] uses a statistical point of view to describe the whole combustion process, which gives a unique approach to combustion problems.

1.2 Objectives

The objective for this studies is to reproduce turbulent pulsed jet flame in RANS/PDF context. The turbulent pulsed jet flame adds an additional flow into a statistical stationary flame, Sydney Flame L. Thus, Sydney Flame L is first studied as a base flame to obtain optimal simulation settings. With the obtained settings, turbulent pulsed jet flame simulations are performed. Critical phenomena observed in experiment are expected to be reproduced during simulations, and preliminary study of the turbulent pulsed jet flame and its extinction gap should be performed.

1.3 Major contributions in this thesis

In this study, following contributions were made:

- Use RANS/PDF method to reproduction of critical phenomena observed in experiment, like extinction and re-ignition.
- Modeling effects and limitations of several mixing models on turbulent pulsed jet flame were discovered and discussed in RANS/PDF context.
- Preliminary analysis of extinction gap location history by comparing experimental data and simulation results.

2. SYDNEY FLAME L AND TURBULENT PULSED JET FLAME

In this chapter, experiment setups of Sydney Flame L and Sydney turbulent pulsed jet flame will be discussed. Both Sydney Flame L and Sydney turbulent pulsed jet flame belong to Sydney piloted flames. Sydney piloted flames is a family of flames on the same burner but with different fuel and fuel velocity. Fig. 2.1 shows one of the piloted flames, Flame D.

Figure 2.1. Image of Sydney piloted flame. [9]

2.1 Sydney Flame L

The turbulent pulsed jet flame is based on Sydney turbulent non-premixed Flame L [10], thus, experiment setups of Sydney Flame L will be discussed first in the following subsections. Parametric studies of this flame was conducted and will be discussed in Chapter 3.

2.1.1 Burner Configuration

The piloted burner developed at the University of Sydney consists of two co-axial tubes [11]. The inner tube is the fuel tube and the outer tube is the piloted tube. Burner sits in the center of a small squared wind tunnel. Fuel, oxidizer and air coming from fuel tube, piloted tube and co-flow wind tunnel exit at the same horizontal plane.

Fuel tube is a stainless steel tube that has length of 550 mm, inner diameter of 7.2 mm and wall thickness of 0.26mm. Pilot tube has outer diameter of 18 mm with lip thickness of 0.2mm. A flame holder consists of 1 mm holes placed 4 mm upstream of the exit plane in pilot tube. Piloted gas inside pilot tube mixed 400 mm upstream of the flame holder. The squared co-flow wind tunnel has sides of 0.3 m with a contraction ratio of 9:1 [12].

2.1.2 Flame Conditions

In Flame L, pure methane CH_4 exit from fuel tube with temperature of 300K and bulk velocity of 41 m/s. Piloted tube has stoichiometric premixed C_2H_2, H_2 and air with C/H ratio the same as methane to form a premixed gas. The unburnt premixed gas comes with temperature of 300 K and bulk velocity of 3 m/s. After the flame holder, burnt gas in piloted tube has a measured velocity of 24 m/s and average temperature around 2600K. Co-flow air from co-flow wind tunnel has temperature of 300 K, velocity of 15 m/s and turbulence level of 2.0% [10].

Flame L data was collected using Spontaneous Raman Scattering [12], a total of 1250 data points was collected at each given location in the flame [10] [13].

Based on previous studies, after leaving the exit plane, flame width will decrease at first. This decreasing is because that high temperature region at this point is caused by the burnt piloted gas. As distance to the exit plane increasing, effect of piloted tube getting weaker. At around $x/D = 10$ (D is the fuel tube diameter) from the jet exit, flame reaches the minimum width and forms a“necking” phenomenon. After passing the “necking” point, the width of flame starts increasing and will expand to about $r/D = 5$ at axial location around $x/D = 60$.

Now, one would have a brief understanding of Sydney Flame L and can move to next section to gain ideas of Sydney turbulent pulsed jet flame.

2.2 Sydney Turbulent Pulsed Jet Flame

In this section, modifications that change Sydney Flame L to Sydney turbulent pulsed jet flame are introduced. The Sydney turbulent pulsed jet flame is based on Sydney Flame L, with variation of velocity added to the fuel tube bulk velocity. Wang et al [14] first introduced this class of statistically transient jet flame. Due to the pulse on bulk velocity of fuel tube, this flame produces extremely complicated combustion dynamics. The flame will break into an upper part and lower part with an extinction gap in between, as shown in fig.2.2. This is because of the pulse introduced flow stretching into this flame. Simulation results in Chapter 5 reproduced the extinction gap with more details.

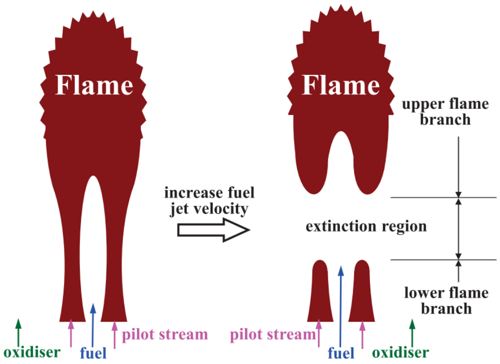

Figure 2.2. Structure of Sydney Pulsed Jet Flame. An extinction gap will present after introducing velocity pulse. [15]

2.2.1 Pulse addition

Pulse of fuel tube velocity is generated as an additional flow to the steady flow of fuel tube. As shown in figure 2.3, the additional flow is supplied by a compressed natural gas (CNG) tank with a pressure regulator controlling supply pressure. Volume between two solenoid valves stores the desired amount of CNG with desired pressure to generate required pulse amplitude. When releasing trapped CNG, valve 1 remains closed with valve 2 opens to inject the trapped high pressure pocket of gas into the main fuel tube.

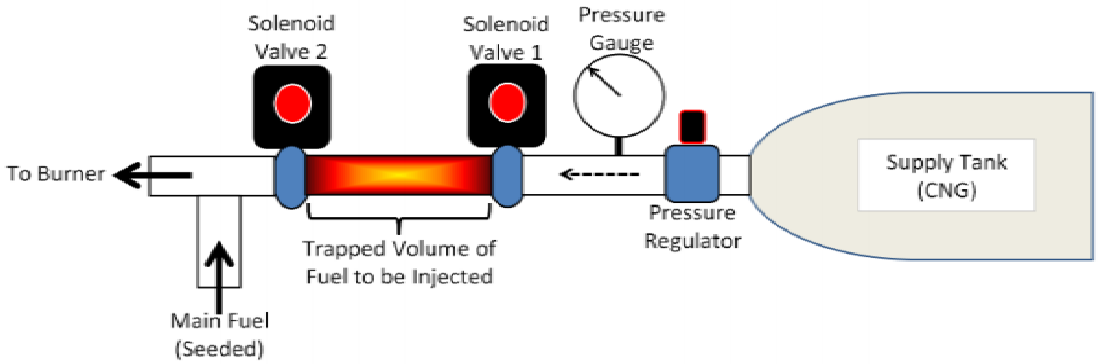

Figure 2.3. Schematic of the pulsing method for the piloted burner showing the fuel supply tank and solenoid valves. [16]

Figure 2.4 shows the centerline velocity at exit plane (x/D=0), and pulse is added at t=10ms. Green dots represent all the data gathered during all 20 pulsed. Red line shows one of the 20 pulsed and black line is the averaged profile of the 20 pulsed. It is noted that due to the non-uniform velocity profile in the fuel tube, steady centerline velocity before 10ms is higher than bulk velocity of 41 m/s.

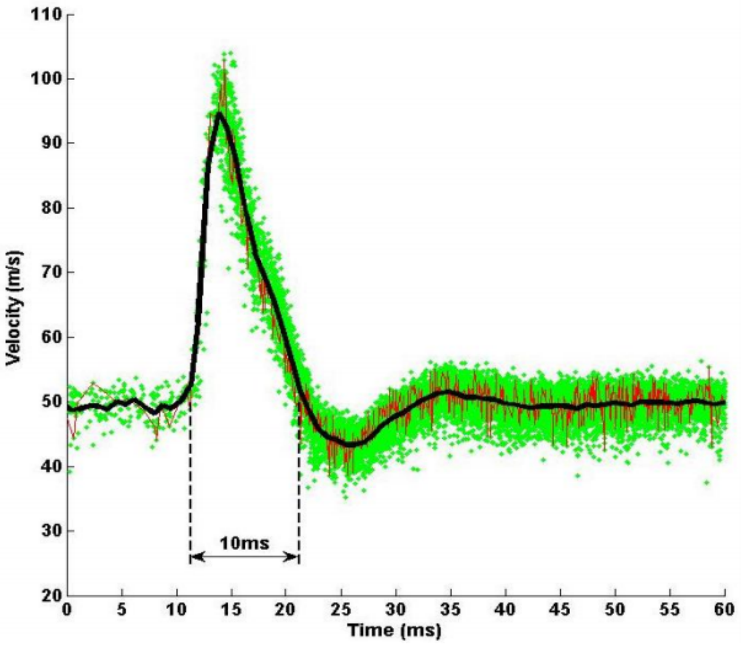

Figure 2.4. A representative scatter plot of twenty velocity time pulses measured on the jet centerline at the exit plane (green dots). The dark (black) line shows the average of the 20 pulses and the thin (red) line shows the trace of a single pulse. [16]

2.2.2 Pulse Time Scale Analysis

Time scale of the pulse is critical to both understanding reaction dynamics and selecting proper modeling approach, so time scale of the pulse is studied in this subsection. Since the pulse is generated by injecting an additional flow to a steady flow, fuel bulk velocity can be represented by a steady part and a time-dependent part in Eq. 2.1.

$$U(t) = U_0(1 + f(t)). \tag{2.1}$$

Curve fitting using Eq. 2.2 is applied to fit $f(t)$ component in Eq. 2.1 with a be a fitting constant and τ_g be the fitted pulse time scale.

$$y(t) = ae^{(t/\tau_g)}. \tag{2.2}$$

Seven data points from averaged data (black line) in Figure 2.4 is presented in Table 2.1. These 7 data points cover from beginning of pulse to peak of pulse. Since actual pulse starts at $t = 10ms$, time for each data point were subtracted so that curve fitting starts at $t = 0$. Time scale of $6.3 \times 10^{-}4$ second is obtained when fitting for all seven data points. However, point 2-4 have the highest increasing rate with a smaller time scale of $3.01 \times 10^{-}4$ second. Based on information above, $3.01 \times 10^{-}4$ second is chosen to be the time scale of this turbulent pulsed jet flame.

Table 2.1. Averaged data points for starting of pulse

Point	Time(ms)	value of f(t)
1	10.0	0.023693
2	10.5	0.009790
3	11.0	0.040775
4	11.5	0.271681
5	12.0	0.447508
6	12.5	0.797166
7	13.0	0.903388

Experimental setups of these two flames have been described. With these setups in mind, one would be comfortable moving to Chapter 3, where modeling approaches and computational methodologies will be discussed.

3. MODELING APPROACHES AND COMPUTATIONAL METHODOLOGIES

3.1 Overview of Modeling Approaches

In Chapter 2, a detailed description of Sydney Flame L and the turbulent pulsed jet flame is provided. In this Chapter, modeling approach and computational methodologies will be introduced. Since flame involves knowledge from turbulence to combustion, modeling will also be presented based on different aspects.

In this study, Reynolds Averaged Navier-Stokes Equation (RANS) with $k-\epsilon$ model [17] was used to calculate the velocity and turbulence fields due to its simplicity and low cost comparing to Large Eddy Simulation (LES). Probability Density Function (PDF) with Monte-Carlo particle method [8] is applied to model combustion process due to its capability to describe chemical reaction process accurately without introducing any assumptions during simulation. A detailed reaction mechanism DRM19 [18] with In Situ Adaptive Tabulation (ISAT) [19–21] are used in this study to perform accurate and fast reaction calculations. Micro-mixing process in composition space are modeled with three mixing models: Interaction by Exchange with the Mean(IEM) [22], Modified Curl model [23] and Euclidean Minimum Spanning Trees(EMST) model [24] in this study.

3.2 RANS $k-\epsilon$ Turbulence Model

The standard RANS $k-\epsilon$ turbulence model was first introduced by Jones and Launder [17]. An assumption of incompressible flow is applied to the RANS equation, but density variation still exist in the simulation since heat release caused large density variation in the flow. The following $k-\epsilon$ model was implemented in this study [25]:

$$\bar{\rho}\frac{Dk}{Dt} = \nabla\left[\left(\mu + \frac{\mu_t}{\sigma_k}\right)\nabla k\right] + P_k - \bar{\rho}\epsilon, \tag{3.1}$$

$$\bar{\rho}\frac{D\epsilon}{Dt} = \nabla\left[\left(\mu + \frac{\mu_t}{\sigma_\epsilon}\right)\nabla \epsilon\right] + (C_{\epsilon 1}P_k - C_{\epsilon 2}\bar{\rho}\epsilon)\frac{\epsilon}{k}, \tag{3.2}$$

$$P_k = -\bar{\rho}\widetilde{u_i''u_j''}\frac{\partial \tilde{u}_i}{\partial \tilde{u}_j}, \tag{3.3}$$

$$-\bar{\rho}\widetilde{u_i''u_j''} = \mu_t\left(\frac{\partial \tilde{u}_i}{\partial x_i} + \frac{\partial \tilde{u}_j}{\partial x_i} - \frac{2}{3}\delta_{ij}\frac{\partial \tilde{u}_k}{\partial x_k}\right) - \frac{2}{3}\bar{\rho}k\delta_{ij}, \tag{3.4}$$

$$\mu_t = C_\mu \bar{\rho}\frac{k^2}{\epsilon}, \tag{3.5}$$

where $\bar{\square}$ denote averaging and $\widetilde{\square}$ denotes Favre averaging. k is the turbulent kinetic energy (TKE), μ is the dynamic viscosity. $C_\mu = 0.09$, $\sigma_k = 1.0$, $\sigma_\epsilon = 1.3$, $C_{\epsilon 1} = 1.44$ and $C_{\epsilon 2} = 1.92$ are the standard model constants for RANS $k - \epsilon$ model.

3.3 PDF method and Monte-Carlo Particle Method

A systematic overview of using Probability Density Function(PDF) method to solve turbulent reactive flow was developed by Stephen B. Pope [8]. PDF method can solve turbulent reactive flows solely by itself, but an alternative approach is also available, which is using turbulent model to solve the velocity field and using PDF method to solve the composition fields. The composition joint PDF is as follows:

$$\bar{\rho}\frac{D\bar{f}}{Dt} = \nabla\left[\left(\bar{\rho}D + \frac{\mu_t}{Sc_t}\right)\nabla\tilde{f}\right] - \frac{\partial}{\partial\Psi_\alpha}\left[\bar{\rho}\tilde{f}S_\alpha(\underline{\Psi})\right] - \frac{\partial^2}{\partial\Psi_\alpha\partial\Psi_\beta}\left[\bar{\rho}\tilde{f}\left\langle D\frac{\partial\phi_\alpha}{\partial x_i}\frac{\partial\phi_\beta}{\partial x_i}|\underline{\Psi}\right\rangle\right], \tag{3.6}$$

where D is the molecular diffusion coefficient. Sc_t is the turbulent Schmidt number. ϕ is the composition vector and Ψ represents composition space. The first term on the right hand side represents molecular and turbulent diffusion of composition PDF in the physical space, with the second term as the source term and the last term is mixing of compositions due to conditional scalar dissipation rate. This PDF is a one-point one-time joint PDF, which does not correlate with another location or time. And the PDF only focuses on the changing of composition field. Velocity field data are taken from RANS $k - \epsilon$ turbulence model mentioned in section 3.2.

In order to solve the PDF equation, Monte Carlo Particle method [26] is employed. Particles which contain mass, volume, temperature and compositions are generated and transported based on velocity field calculated from RANS simulation.

3.4 Detailed Reaction Mechanism with ISAT

In this study, chemical source term $S_\alpha(\underline{\Psi})$ is calculated using DRM 19 chemical reaction mechanism with In Situ Adaptive Tabulation (ISAT).

DRM19 is a reduced mechanism with 19 species based on GRI Mech 1.2 [18]. It is developed with the object of using smallest set of reactions to reproduce the same main combustion characteristics as GRI-Mech 1.2 with acceptable accuracy loss(6-8% respect to GRI-Mech).

ISAT [19] is also applied in the calculation of chemical reactions. This technique was developed to increase computational efficiency of detailed chemistry reaction. Due to the characteristics of the unique differential equations which governs chemical reaction, methodologies developed in ISAT accelerating calculation of the reaction source term. When comparing to direct solving chemical reactions, approximately speed-up factor of 7.5 can be achieved. When implemented into PDF methods, ISAT is much simpler and also much more effective and can speed-ups of 100-1000 [19].

3.5 Mixing Models

The last term of Eq.3.6, $\frac{\partial^2}{\partial\Psi_\alpha\partial\Psi_\beta}\left[\bar{\rho}\tilde{f}\left\langle D\frac{\partial\phi_\alpha}{\partial x_i}\frac{\partial\phi_\beta}{\partial x_i}|\underline{\Psi}\right\rangle\right]$ is not closed and needs to be modeled. This term is the dissipation of conditional scalar that related to molecular mixing. There are several mixing models available for this molecular mixing, which the three commonly used models are IEM [22], Modified Curl [23] and EMST model [24].

3.5.1 IEM Mixing Model

IEM(Interaction by Exchange with the Mean) mixing model was introduced by Villermaux and Devillon [22]. Main concept of this model is to advance composition on a particle towards mean value. This model can be described by ordinary differential equation,

$$\frac{d\phi^n}{dt} = -\frac{1}{2} C_\phi \frac{\epsilon}{k} \Big(\phi^n - \tilde{\phi} \Big), \tag{3.7}$$

where ϕ^n denotes scalar on nth particle and $\tilde{\phi}$ is Favre averaged composition of the ensemble of particles. By exchange with mean, scalar variance decreased which represents dissipation of variance. However, due to the fact that mixing is performed with all other particles in a cell, this model is lack of localness.

3.5.2 MCurl Mixing Model

Modified Curl mixing model is a particle interaction model based on Curl's mixing model [27]. Different from the IEM model that exchange compositions with mean, multiple pairs of particles are selected in Modified Curl mixing model and exchange compositions based on the following equation:

$$\phi^{p,new} = \phi^p + \frac{1}{2} a \Big(\phi^q - \phi^p \Big), \tag{3.8}$$

$$\phi^{q,new} = \phi^q + \frac{1}{2} a \Big(\phi^p - \phi^q \Big), \tag{3.9}$$

where a can be a number between 0 and 1.Eq.(3.8-3.9) are for equal weighted particle pairs. For unequal weighted particle pairs, Nooren et al. [28] developed an implementation of Modified Curl mixing model:

$$\phi^{p,new} = \phi^{q,new} = \frac{1}{w^p + w^q} \Big(w^p \phi^p + w^q \phi^q \Big), \tag{3.10}$$

which corresponding to $a = 1$ for Eq.(3.8-3.9) with w represents particle weights. Number of pairs of particles selected is controlled by mixing coefficient C_ϕ so that same C_ϕ will have the same decay rate of variance as that in IEM mixing model.

3.5.3 EMST Mixing Model

The EMST mixing model is developed based on the Euclidean Minimum Spanning Tree which connect all particles with the minimum distance in the composition field.

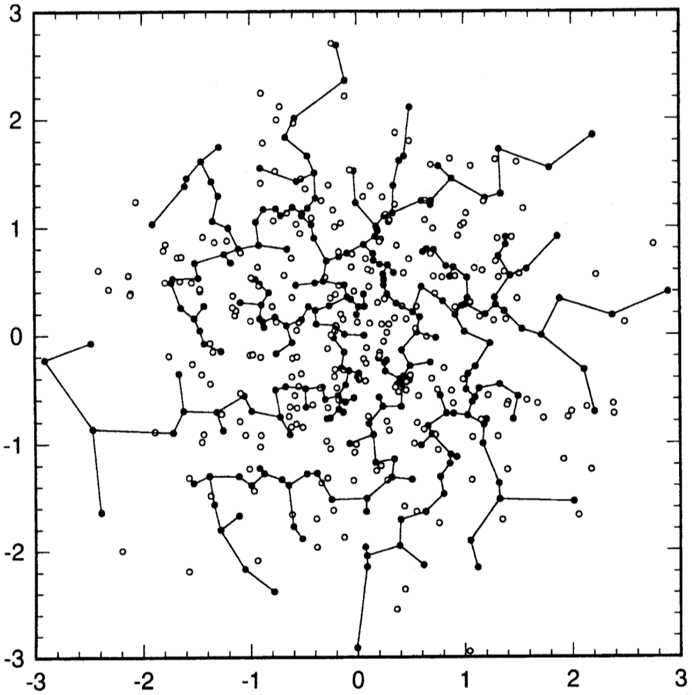

Figure 3.1. N=512 joint-normal distribution particles in a 2-D space connected by Euclidean Minimum Spanning Tree(EMST). Filled dots represents particles in mixing stage while unfilled dots represents particles in non-mixing stage [24].

Let w denote particle weight and W denote edge weight. Each particle has a weight w_i and each edge connect two particles m and n. If one edge is removed, the rest particle will form two set of particles S_m, S_n that connect through two minimum spanning tree(MST). The sum of the weight of particles in two MST can be denoted as:

$$w_{S_m} = \sum_{i \in W_m} w_i, \tag{3.11}$$

$$w_{S_n} = \sum_{i \in W_n} w_i. \tag{3.12}$$

Now, edge weight of this specific edge k can be defined as:

$$W_k = min\Big(w_{S_m}, w_{S_n}\Big). \tag{3.13}$$

Since the sum of all particles is unity, which give the range for edge weight from the minimum particle weight to 1/2. A edge coefficient is chosen as a linear function of the edge weight:

$$B_k = 2W_k. \tag{3.14}$$

Based on the edge coefficient, an interaction matrix can be defined as:

$$M_{ij} = -\alpha \sum_{k=1}^{N_p-1} B_k\Big(\delta_{im_k}\delta_{jn_k} + \delta_{jm_k}\delta_{in_k}\Big), j \neq i, \tag{3.15}$$

$$M_{(i)(i)} = -\alpha \sum_{j=1}^{N_p} \sum_{k=1}^{N_p-1} B_k\Big(\delta_{im_k}\delta_{jn_k} + \delta_{jm_k}\delta_{in_k}\Big), \tag{3.16}$$

with N_p is the number of particles and δ represents the Kronecker delta. Model parameter α controls the decaying rate of variance. It is chosen in a way that EMST model will perform the same decaying rate as other mixing models. Then the EMST model evolution equation can be written as:

$$\frac{d\phi_{\beta i}}{dt} = -\frac{1}{w_i} M_{ij}\phi_{\beta j}, i = 1, ..., N_p, \tag{3.17}$$

where $\phi_{\beta i}$ represents the βth composition on ith particle.

Particle aging technique is also applied in EMST model to prevent "stranding" effect which if all particles are evolved in all steps of mixing, particles will move along specific branches due to specific path generated using minimum spanning tree.

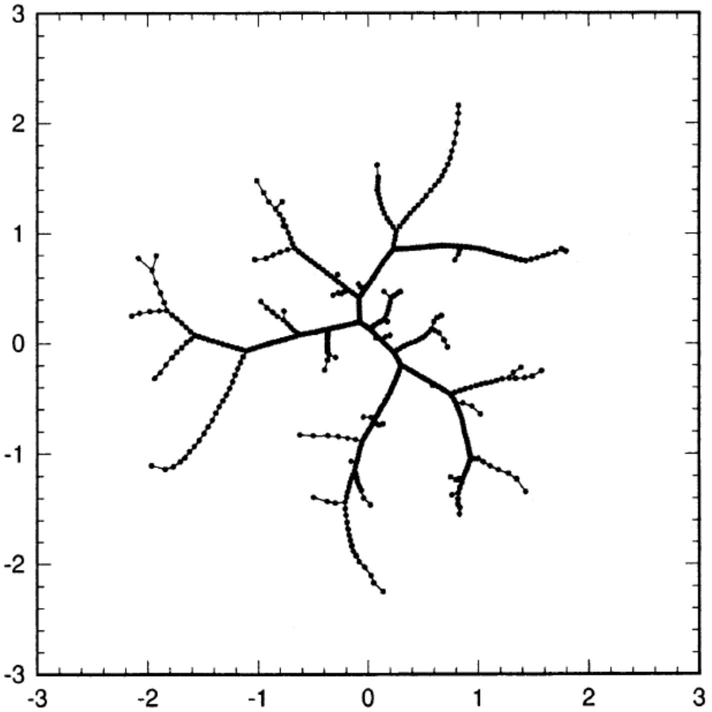

Figure 3.2. Scatter plot of particles histories in 2-D composition space with "stranding" effect, initially distributed as joint normal distribution [24].

As shown in fig.3.2, as mixing proceeds, particle histories form a specific pathway along minimum spanning tree and a given particle will only attract and interact with same particles around it. This is not consistent with the physics of mixing where particles move around the domain while interacting with all the particles, that, particle path histories should not be unique.

Particle aging technique was developed based on this concept. A scaled time was defined in terms of mean turbulent coefficient ($< \omega >$), physical time t and an arbitrary fixed origin of scaled time s_0:

$$s \equiv S_0 + \int_0^t < \omega > (t) dt. \tag{3.18}$$

Particle age is advanced based on the following equations with infinitesimal positive ds :

$$Z(s+ds) = Z(s) - ds,\ for\ Z(s) > ds, \tag{3.19}$$

$$Z(s+ds) = Z(s) + ds,\ for\ Z(s) < -ds, \tag{3.20}$$

$$Z(s+ds) = U_1(z),\ for\ 0 \leq Z(s) \leq ds, \tag{3.21}$$

$$Z(s+ds) = U_0(z),\ for\ -ds \leq Z(s) \leq 0, \tag{3.22}$$

where $U_1(z)$ and $U_0(z)$ are random function that uniformly distributed on $\big[Z_{1l}, Z_{1u}\big]$ and $\big[-Z_{0u}, -Z_{0l}\big]$ respectively. An example of age history of a particle in given as fig.3.3.

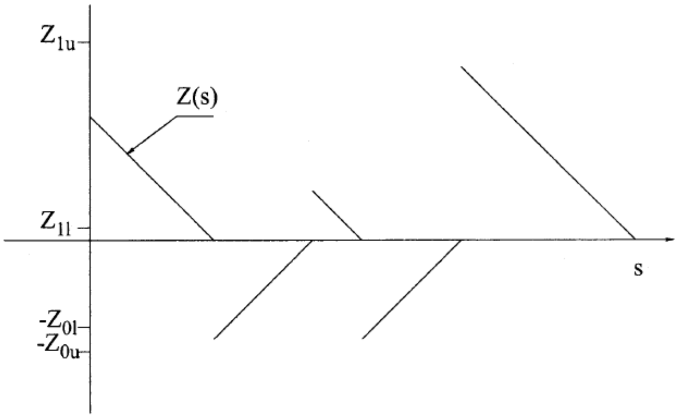

Figure 3.3. An example of age history of a particle [24].

This particle started in mixing state ($Z(s) > 0$). When it reaches $0 \leq Z(s) \leq ds$, it is given a random number in the range of $\big[-Z_0u, -Z_0l\big]$ so that it entered non-mixing state. It's state keeping repeating between mixing and non-mixing state as time advances.

3.6 Computational Methodology

In this section, general information of computational methodology employed in this study will be discussed. A Fortran turbulence velocity solver coupled with HPDF code [29] is used to perform simulations for this study. The code can achieve second order accuracy both in space and time. For parallel computing, parallelization can be achieved by decomposing computational domain in two directions and can handle up to 4096 cores.

3.6.1 Computational Domain and grid spacing

Previous studies on Flame L and turbulent pulsed jet flame [15] used a domain size of $20D \times 60D$ from exit plane of fuel tube and pilot tube, where $20D$ is in radial direction and $60D$ is in axial direction. This domain is proved that it can well reproduce the Flame L so it is employed in this study. The Flame will only expand to around $r/D = 5$ but entrainment of air will affect computational results if the domain is too small. $20D$ is commonly used in simulating these series of flames, with this size, entrainment is almost negligible. Experimental data of velocity fields have data to the point of $x/D = 50$, so $x/D = 60$ is chosen as axial direction domain size.

Grids are particularly refined near the jet exit plane to resolve the mixing layers.Since fuel tube and pilot tube ends at the exit plane, grid size near these two wall also needs also to be small.

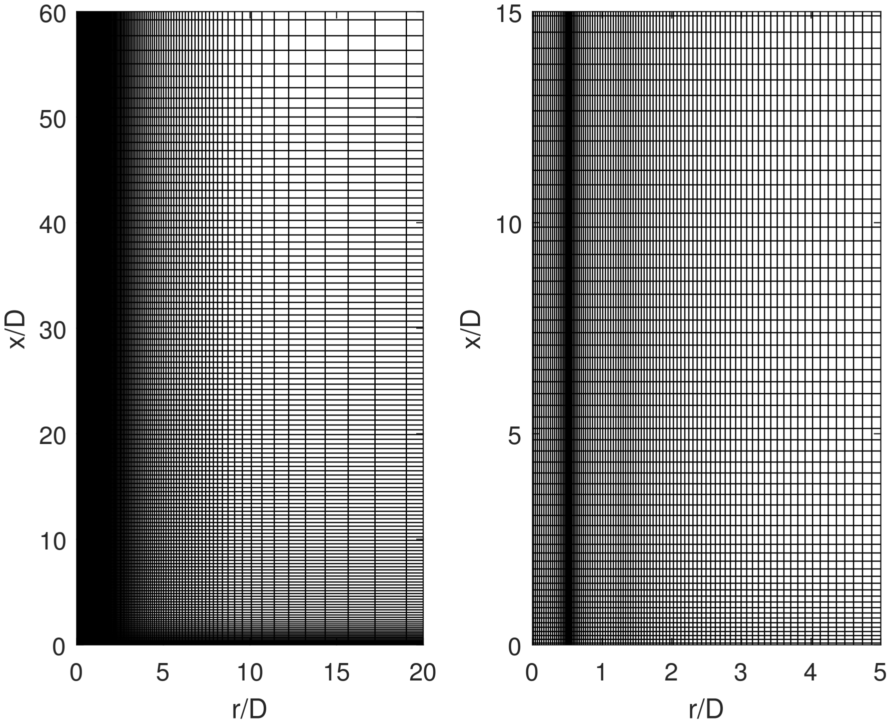

Figure 3.4. Grid for computational domain. Subplot on left is the Whole domain, subplot on right is zoomed in for closer view.

This grid spacing in axial and radial directions have been used in LES/PDF studies by Zhang et al. [15] and proved to be able to resolve Flame L and Pulse Jet Flame in quite well.

3.6.2 Inlet and Boundary Condition for Computational Domain

Inlet and boundary condition for this study consists fuel tube inlet, pilot tube inlet, co-flow inlet, side outlet and end outlet.

For fuel tube inlet condition, the Reynolds number of fuel flow is around 17000. The mean velocity profile applied here follows a DNS calculation contains only the fuel tube, and this profile yields bulk velocity of $41m/s$. Turbulent kinetic energy(TKE) and dissipation are tabulated based on a separate simulation of pipe flow with the same mean velocity. Since pure methane is used as fuel, inlet condition of composition in fuel tube has methane with mixture fraction $\xi = 1$ at $T = 300K$.

Pilot tube has a mixture of C_2H_2, H_2 and air with the same C/H ratio as methane(CH_4) and the mixture is at the stoichiometric condition or the equivalence ratio equals 1. This mixture comes to pilot tube at $T = 300k$ and bulk velocity of $3m/s$ before burnt. After assumptions of 5% heat loss in the burning stage and uniform velocity at the exit of pilot tube, temperature of $2354.29K$, Velocity of $21.9331m/s$ and properties in table 3.1 are calculated.

Co-flow inlet condition has parabolic mean velocity profile near pilot tube wall with a boundary layer thickness of $1.94D$ or $0.01397m$. The uniform mean axial velocity is $U = 15m/s$. Composition of co-flow is the same as standard air.

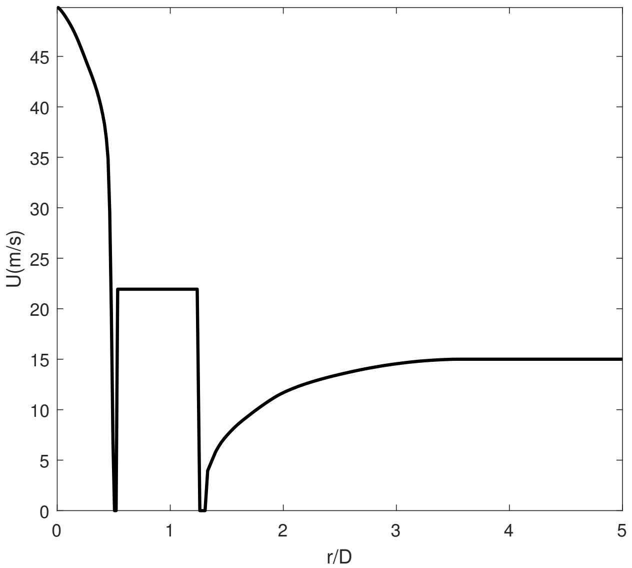

Figure 3.5. Inlet mean velocity(m/s) at the exit plane of fuel tube and pilot tube. Computational domain starts at exit plane. Wall of fuel tube and pilot tube have mean velocity of zero.

Fig.3.5 shows mean axial velocity of all three inlets mentioned above. Mean axial velocity in the fuel tube various but keeps bulk velocity as $41m/s$. With mean axial

Table 3.1. Inflow composition of pilot tube

Species	Mass Fraction
H_2	6.3806e-04
H	7.8799e-05
O	8.5585e-04
O_2	1.4661e-02
OH	5.5827e-03
H_2O	1.1870e-01
HO_2	2.6408e-6
CH_2	2.7299e-16
CH_2(S)	2.0270e-17
CH_3	7.3679e-16
CH_4	1.7724e-16
CO	2.1806e-02
CO_2	1.1636e-01
HCO	7.0902e-09
CH_2O	8.1147e-11
CH_3O	1.2919e-17
C_2H_4	4.0098e-25
C_2H_5	9.8791e-30
C_2H_6	3.7513e-31
N_2	7.2132e-01

velocity at two walls decrease to zero. Co-flow mean axial velocity will keep as $15m/s$ for $r/D > 5$. For outlet at $r/D = 20$ and $x/D = 60$, both outlet only allow outflow, back flow is not permitted in this study.

For turbulent pulsed jet flame, velocity pulse function will be added to the fuel tube velocity field using the flowing functions:

$$U(t) = U_0(1 + f(t)) \tag{3.23}$$

$$V(t) = V_0(1 + f(t)) \tag{3.24}$$

$$W(t) = W_0(1 + f(t)) \tag{3.25}$$

$$k(t) = k_0(1 + f(t))^2 \tag{3.26}$$

$$\epsilon(t) = \epsilon_0(1 + f(t))^3 \tag{3.27}$$

3.6.3 Moving Time Averaging(MTA)

Due to the nature of PDF method, PDF simulations will never reach to a steady state for Flame L. Results from PDF simulations will only reach statistical stationary state. For flames calculations, the fluctuation range can be large, which is not acceptable for RANS simulation. So moving time averaging(MTA) [30] technique is also implemented in this code to suppress fluctuation of RANS/PDF calculations:

$$\phi_{TA}^{n+1} = \left(1 - \frac{1}{NTA}\right)\phi_{TA}^{n} + \frac{1}{NTA}\phi^{n+1}. \tag{3.28}$$

In every time step when a scalar gets a new instantaneous value ϕ^{n+1} from calculation, it averages with the old time averaged value ϕ_{TA}^{n} by a control coefficient NTA. The NTA number represents the equivalent averaging steps. When $NTA = 1$, the new value is not averaging with old value at all.

This moving time averaging not only controls the fluctuation, but also affects implementation of pulse, which will be discussed in section 4.4.

4. PARAMETRIC STUDIES OF FLAME L

In this chapter, parametric studies of Flame L will be discussed. Grid independent study and effect of $C_{\epsilon 1}$, Sc, mixing models, mixing coefficients, NTA numbers and particle numbers are studied. Optimal settings determined from these parametric studies will be served to simulate turbulent pulsed jet flame accurately. Results from pulsed jet flame will be discussed in Chapter 5.

4.1 Grid Independent Study

A grid convergence study for the whole domain is presented in section 4.1.1 with six different numbers of grid points. Convergence trend is observed and a moderate grid is chosen to proceed. Another grid refinement study in section 4.1.2 is focus on out region of the flame when results variation in that region is observed in section 4.4.

4.1.1 Grid Convergence Study

With the setups discussed in Chapter 3, simulation can be successfully performed. For grid convergence study, a total of 6 sets of grids are used ($64 \times 64 \times 1, 96 \times 96 \times 1, 128 \times 128 \times 1, 144 \times 144 \times 1, 160 \times 160 \times 1, 192 \times 192 \times 1$) to perform calculation for Flame L. Multiple grid points in the azimuthal direction will report the same result as one grid points in RANS/PDF context, so only one cell is used in azimuthal direction to reduce computational cost. Although different number of grid points are used here, the percentage of grid points in a section(exp. fuel tube) remain the same as total grid point increase in this grid convergence study.

Fig.4.1 shows convergence history of density from simulation with $192 \times 192 \times 1$ grid. It is also a time history since all simulations in this study are transient and advancing in time. Statistics is calculated based on data collected after flow field has reached a statistical stationary state. For this case shown in fig.4.1, statistics is calculated based on data collected after 24000 steps.

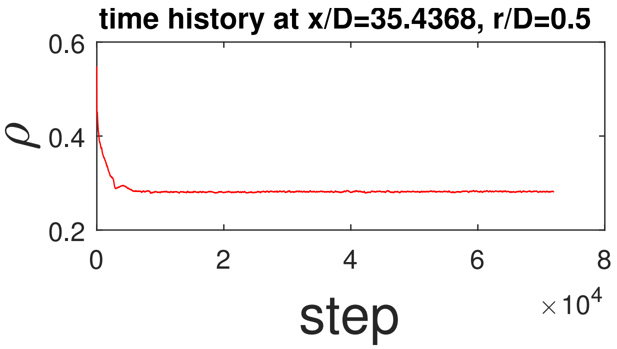

Figure 4.1. Time history of density at a given location on $192 \times 192 \times 1$ grid.

Fig. 4.2-4.4 are radial profiles of mean axial velocity (U), mean temperature (T) and fuel mixture fraction ξ. From these radial profiles, one can tell that most of the results are highly overlapped with each other. Except for case with $192 \times 192 \times 1$ number of grid cells, differences between its profile and other cases at far downstream $(x/D = 50)$ and out region of the flame $(r/D = 3)$ can be observed.

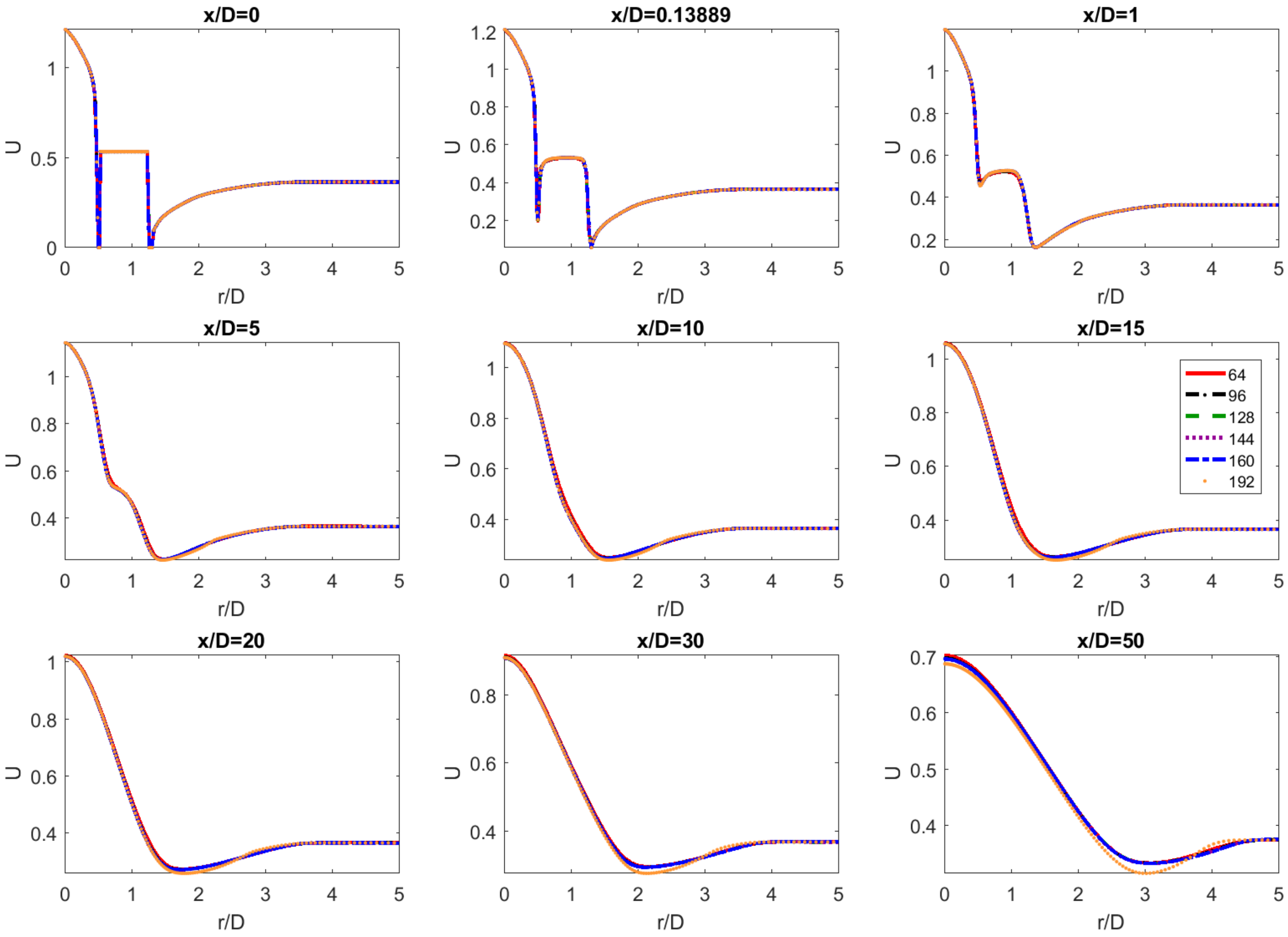

Figure 4.2. Radial profile of normalized mean axial velocity U at 9 different axial locations for cases with different grid number.

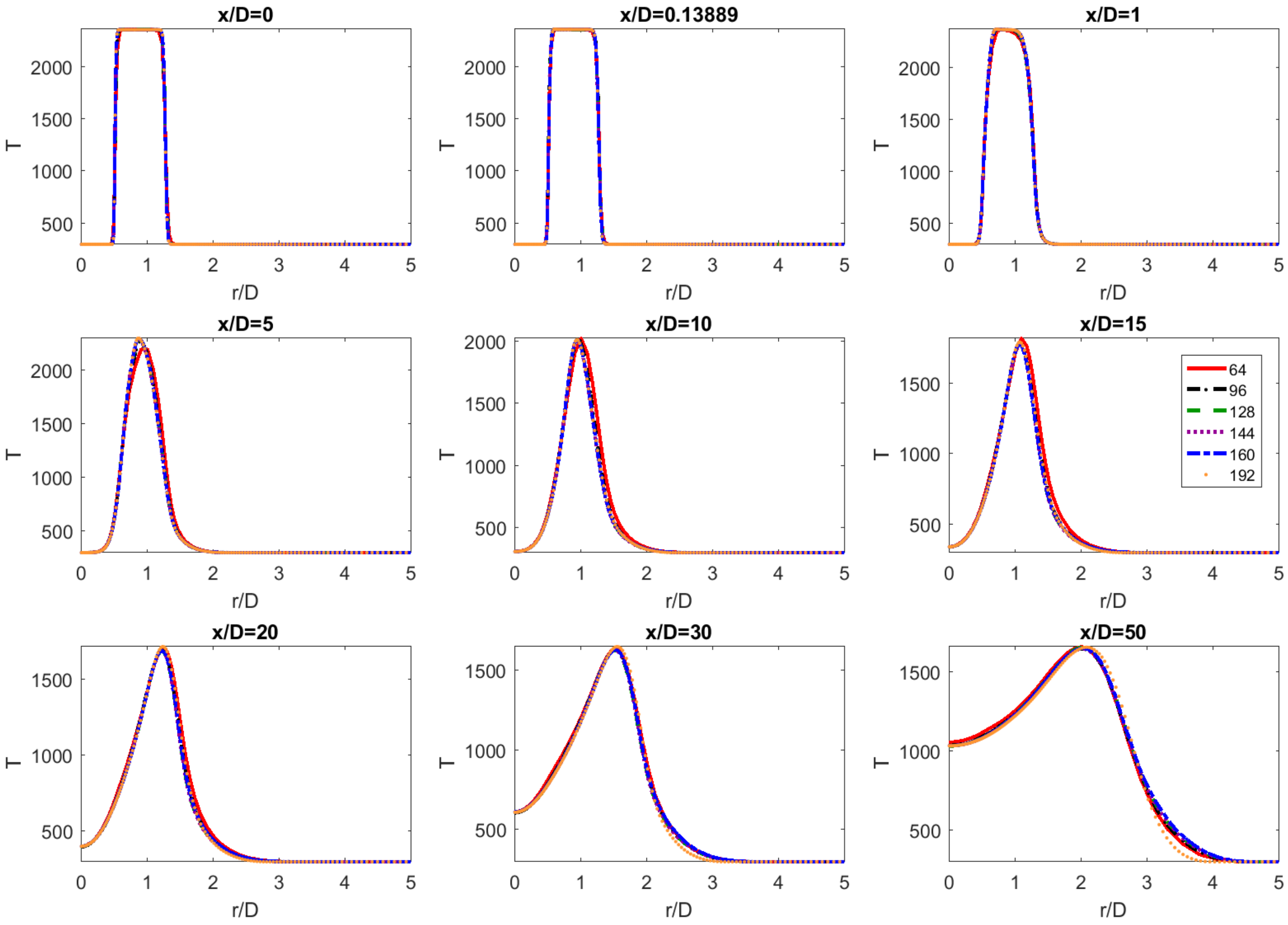

Figure 4.3. Radial profile of mean Temperature at 9 different axial locations for cases with different grid number.

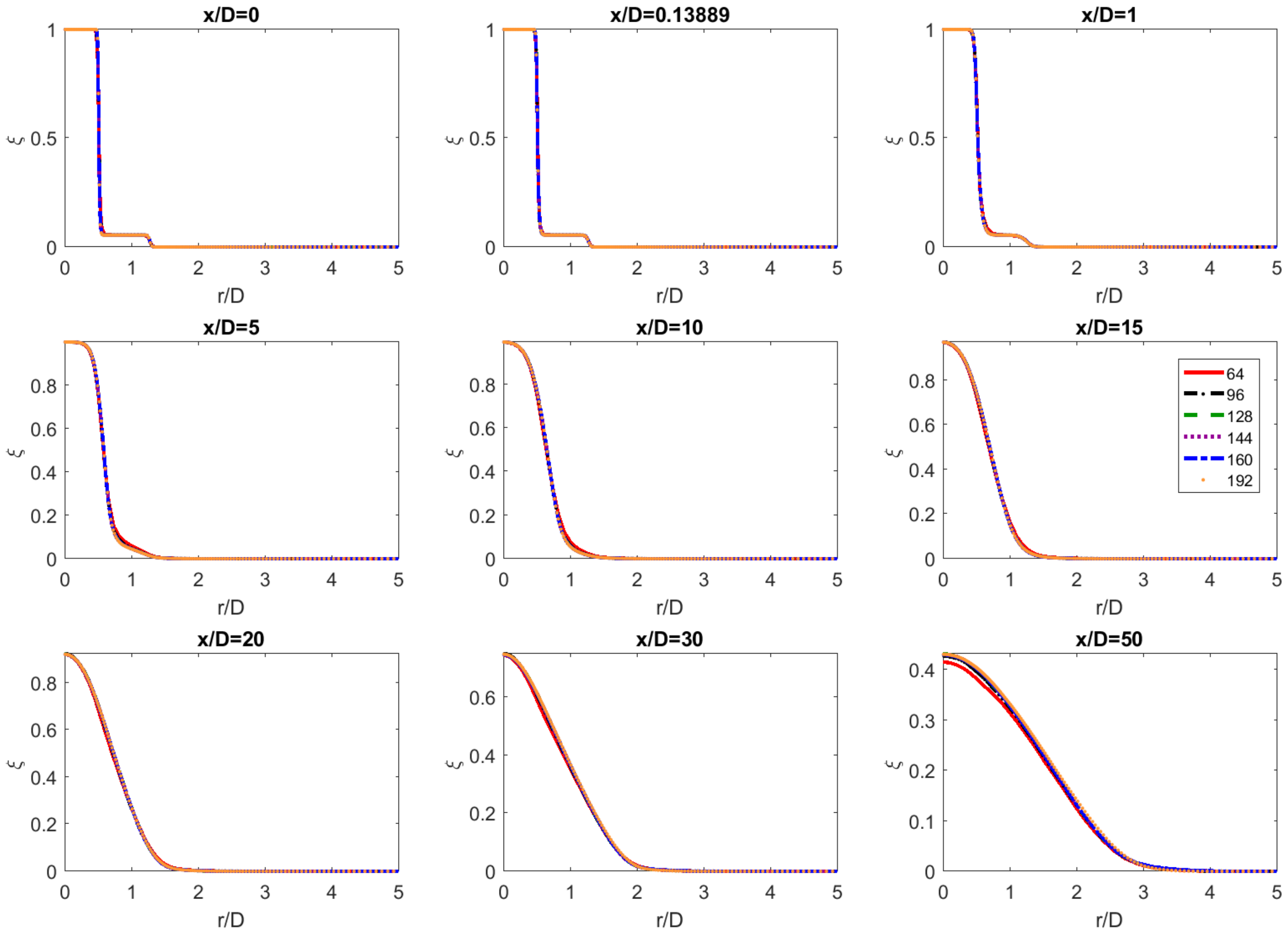

Figure 4.4. Radial profile of mean mixture fraction at 9 different axial locations for cases with different grid number.

Fig. 4.5-4.7 shows relative error of U, T and ξ. Relative error for grid convergence study is calculated using the following equation:

$$error_{relative} = \frac{|\phi_{target} - \phi|}{\phi_{globalmaximum}} \tag{4.1}$$

Relative errors are plotted against the inverse of number of grid cells, which will decrease when number of grid cells increases. Usually a linear curve fitting can be performed. Intersection of this curve and vertical axis is assumed to be a simulation result with no domain discretization error(ϕ_{target}). However, since linear relation of relative error and grid size is not clearly presented in some locations, results from $192 \times 192 \times 1$ grid is used as ϕ_{target}. As presented in the relative error scatter plots fig.4.4-4.6, relative error of all results stay below 5%. It is evident that different variables have good convergence trend in the center of flame ($r/D < 1.8$). For locations where convergence trend is hardly observed, relative error is too small in terms of order of magnitudes.

Based on results presented, increasing number of grid cells do show convergence trend for different variables at given locations. All grids tested in this gird convergence study have small relative error ($\leq 5\%$ when compares to value from $192 \times 192 \times 1$ case). $128 \times 128 \times 1$ is chosen as the standard grid for all the following calculations due to the fact that it has low computational cost and can yield reasonable accurate results.

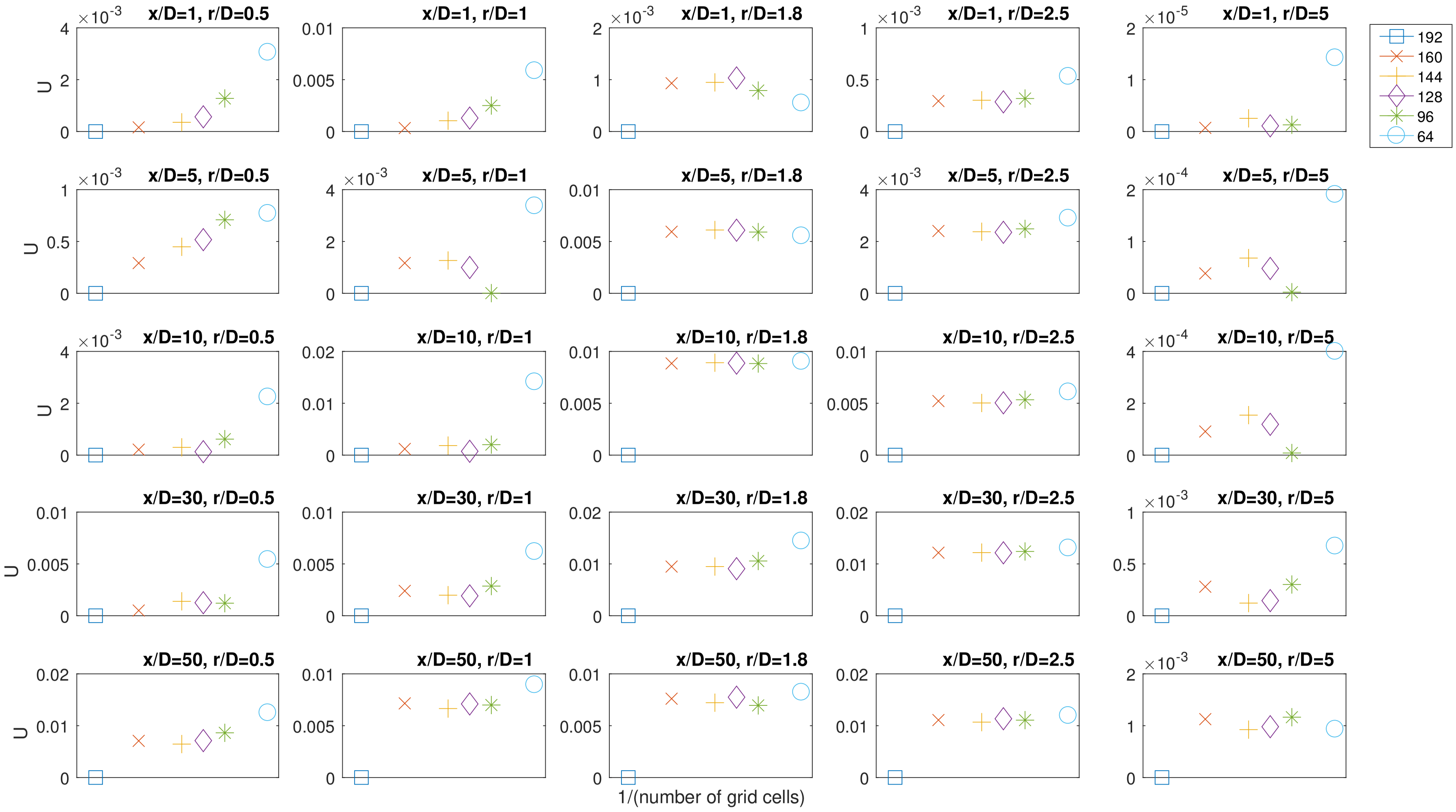

Figure 4.5. Scatter plots of normalized mean axial velocity U relative error versus inverse of number of grid cells at 25 selected locations.

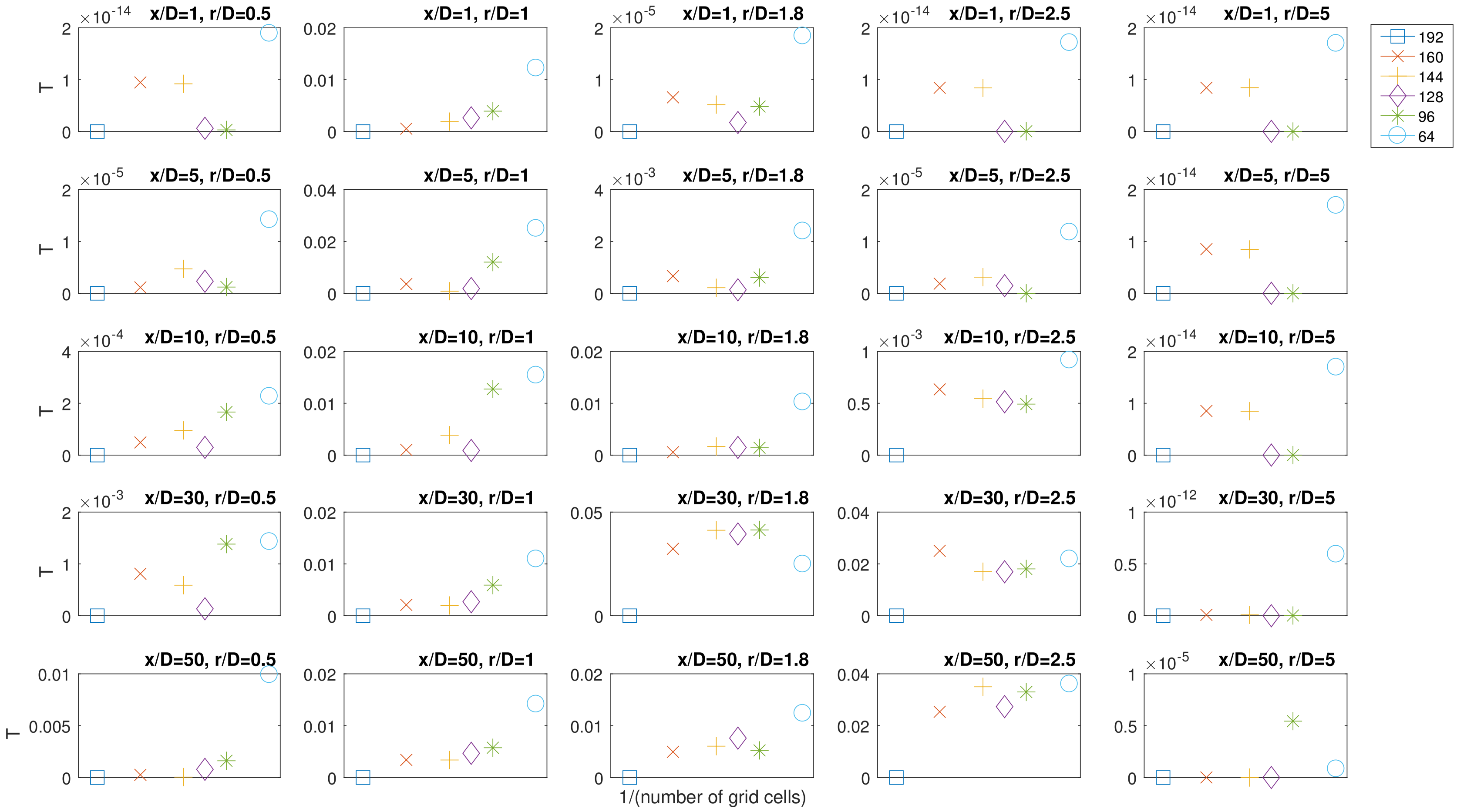

Figure 4.6. Scatter plots of mean Temperature relative error versus inverse of number of grid cells at 25 selected locations.

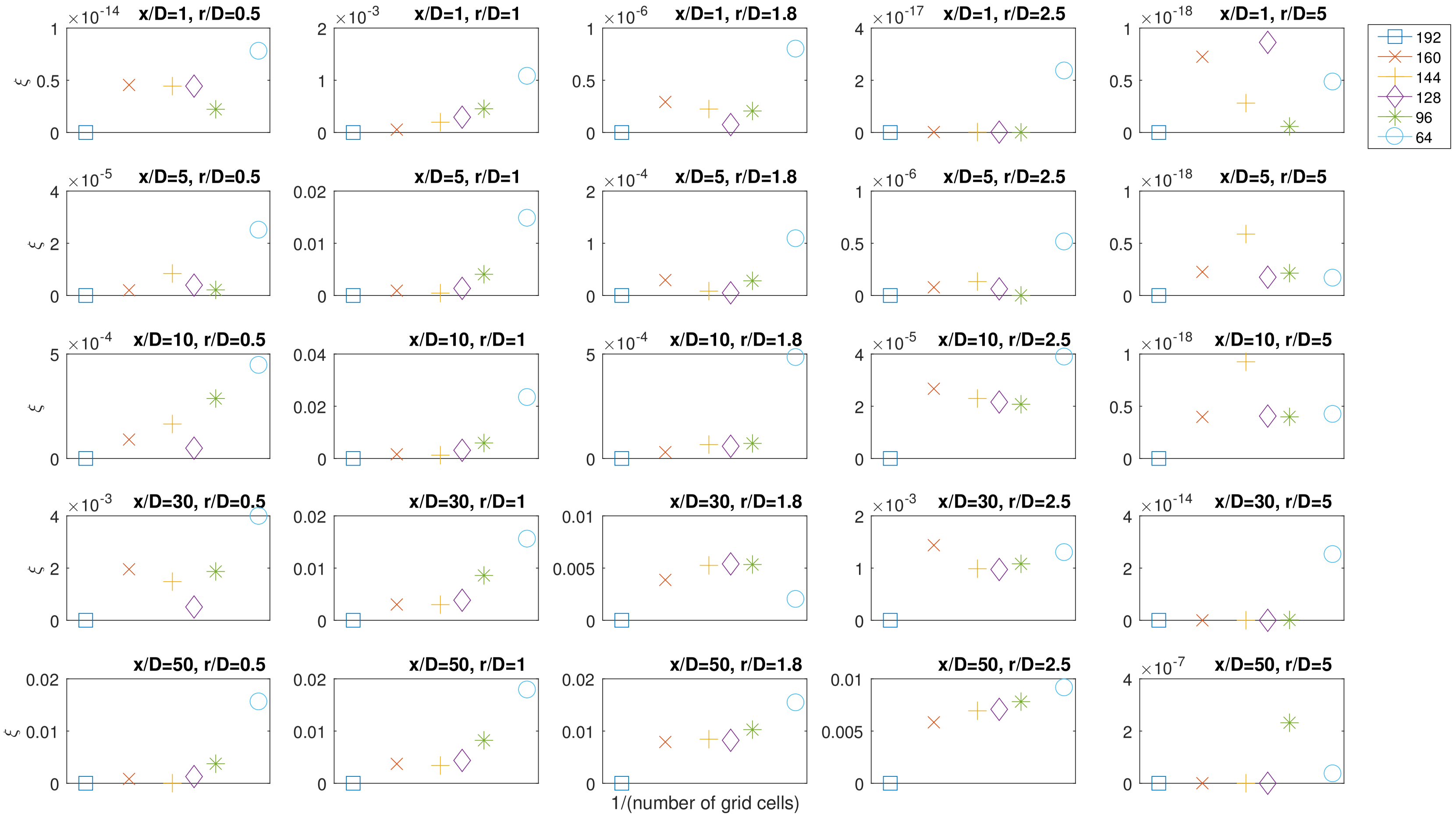

Figure 4.7. Scatter plots of mean mixture fraction relative error versus inverse of number of grid cells at 25 selected locations.

4.1.2 Refinement Study

Beside the grid convergence study of the whole domain, another grid study presented in this study is a refinement study for outer region of the flame. In section 4.4, when testing various effective particle number $N_{pc,eff}$, results from those cases are similar inside the flame but various a lot at outer region $r/D > 2$. The grid refinement study presented here is to answer whether a refined grid in needed or not.

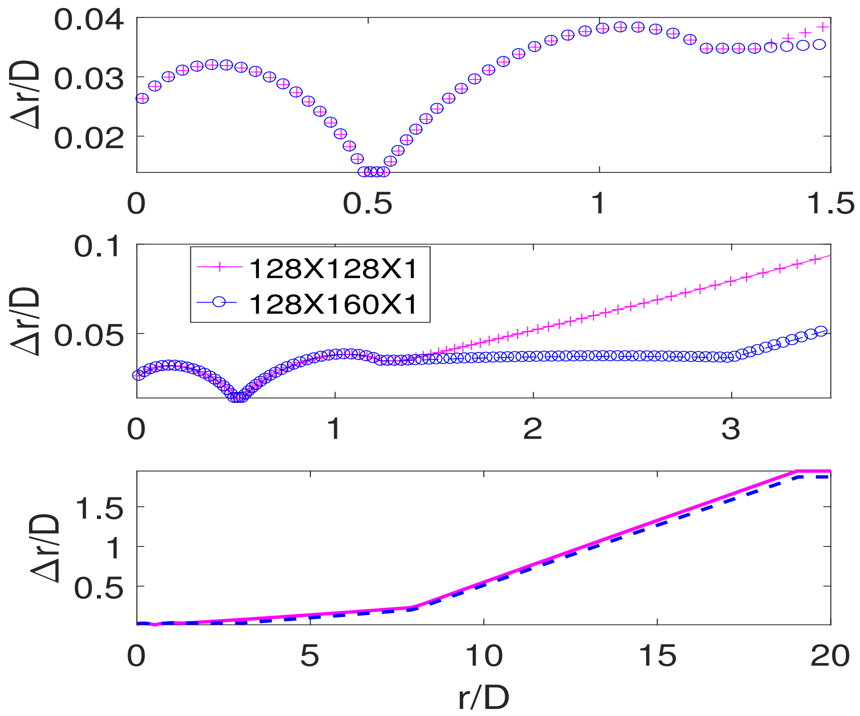

Figure 4.8. Grid spacing of standard grid and refined grid in radial direction. $128 \times 160 \times 1$ is the refined grid that adds more grid points in $r/D \in [1.25, 3]$.

Fig. 4.8 shows the grid spacing in radial direction for both standard grid and refined grid. Fuel tube and pilot tube are in region $r/D \in [0, 1.25]$. Number of gird cells in the refined grid stays the same as standard grid in this region so that refinement will only apply to outer region.

Grid size starts increasing at $r/D > 1.25$ for standard gird. One concern here is that the ratio of two neighboring cell sizes might cause the variation that observed in section 4.4. Refinement did here delays the increasing of spacing after $r/D = 3$ so that there's no dramatically change to size of grid cells. Fig. 4.9 shows the outlooks of standard grid and refined grid.

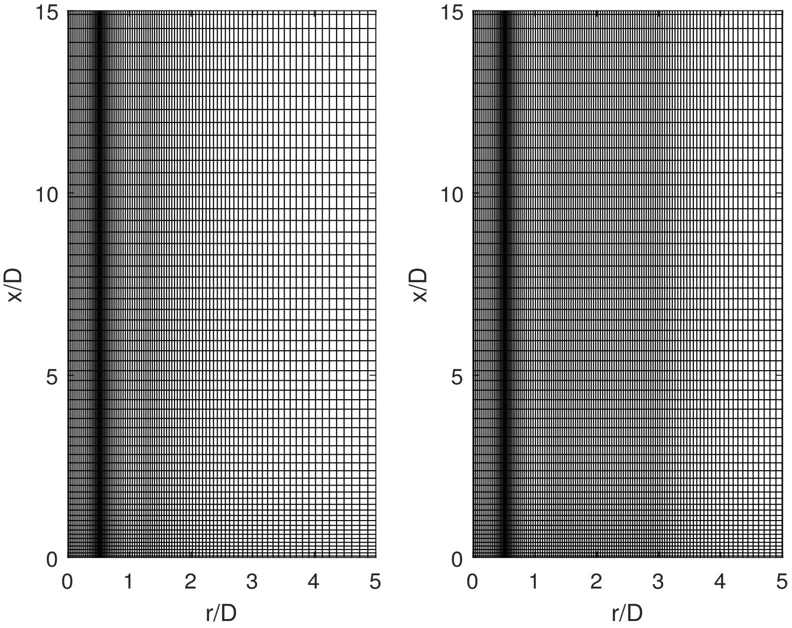

Figure 4.9. Standard grid (left) and refined grid (right). Refinement generate more cells in $r/D \in$[1.25 3].

Comparison of results from standard grid and refined grid are presented in Fig. 4.10-4.12. Radial profiles of minimum and maximum NTA numbers with their results from both standard and refined grid are presented. Blue lines are results from standard grid and red lines are from refined grid. Results from both grid are highly overlapped except only small difference is observed in radial profile of mean radial velocity V. This can conclude that grid spacing does not contribute to results variation in cases with different effective particle number $N_{pc,eff}$. With the above conclusion, standard gird $128 \times 128 \times 1$ continued to be used in the following calculations.

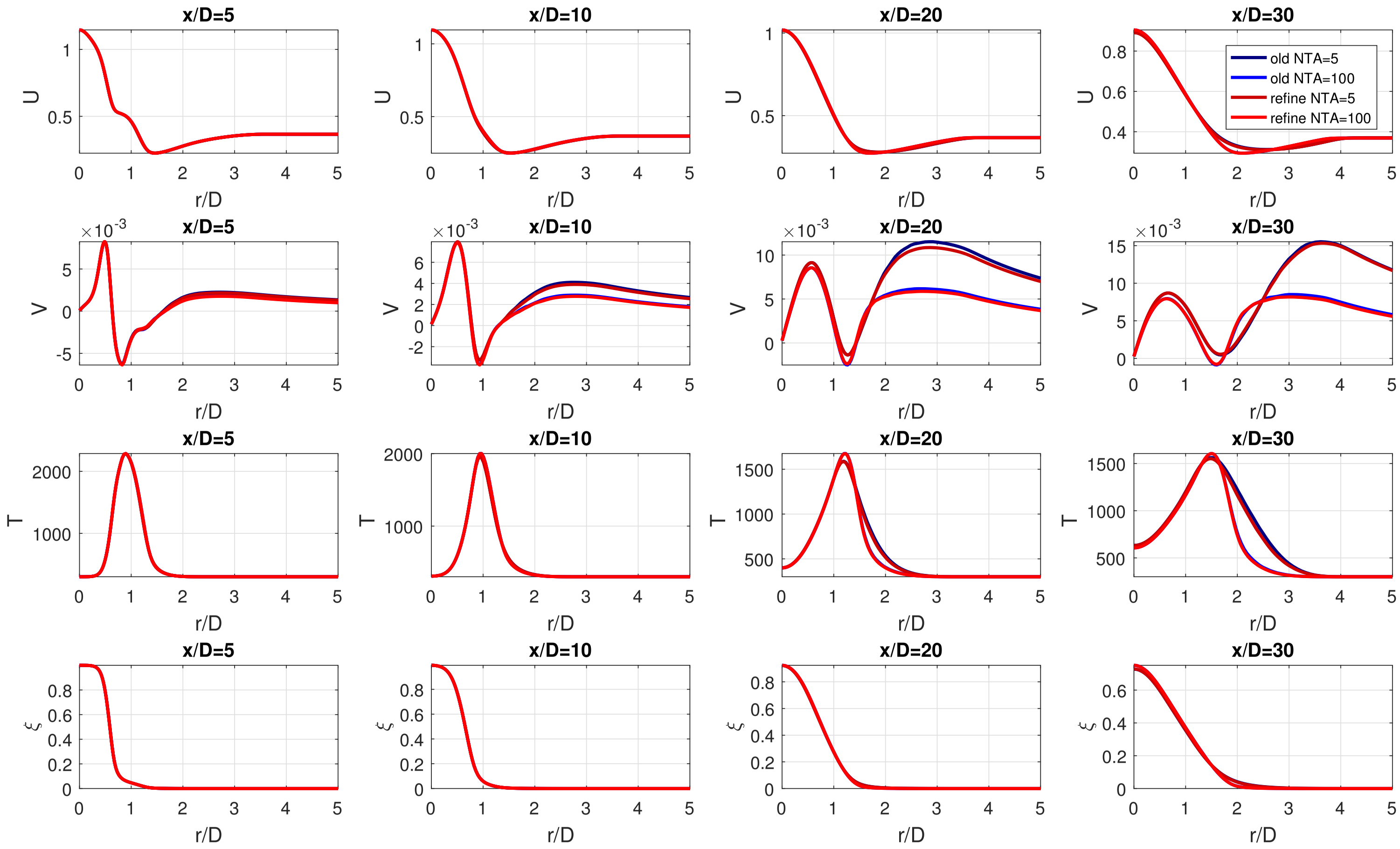

Figure 4.10. Radial profiles of U, V, T and ξ with NTA=5 and NTA=100 cases on both standard and refined grid.

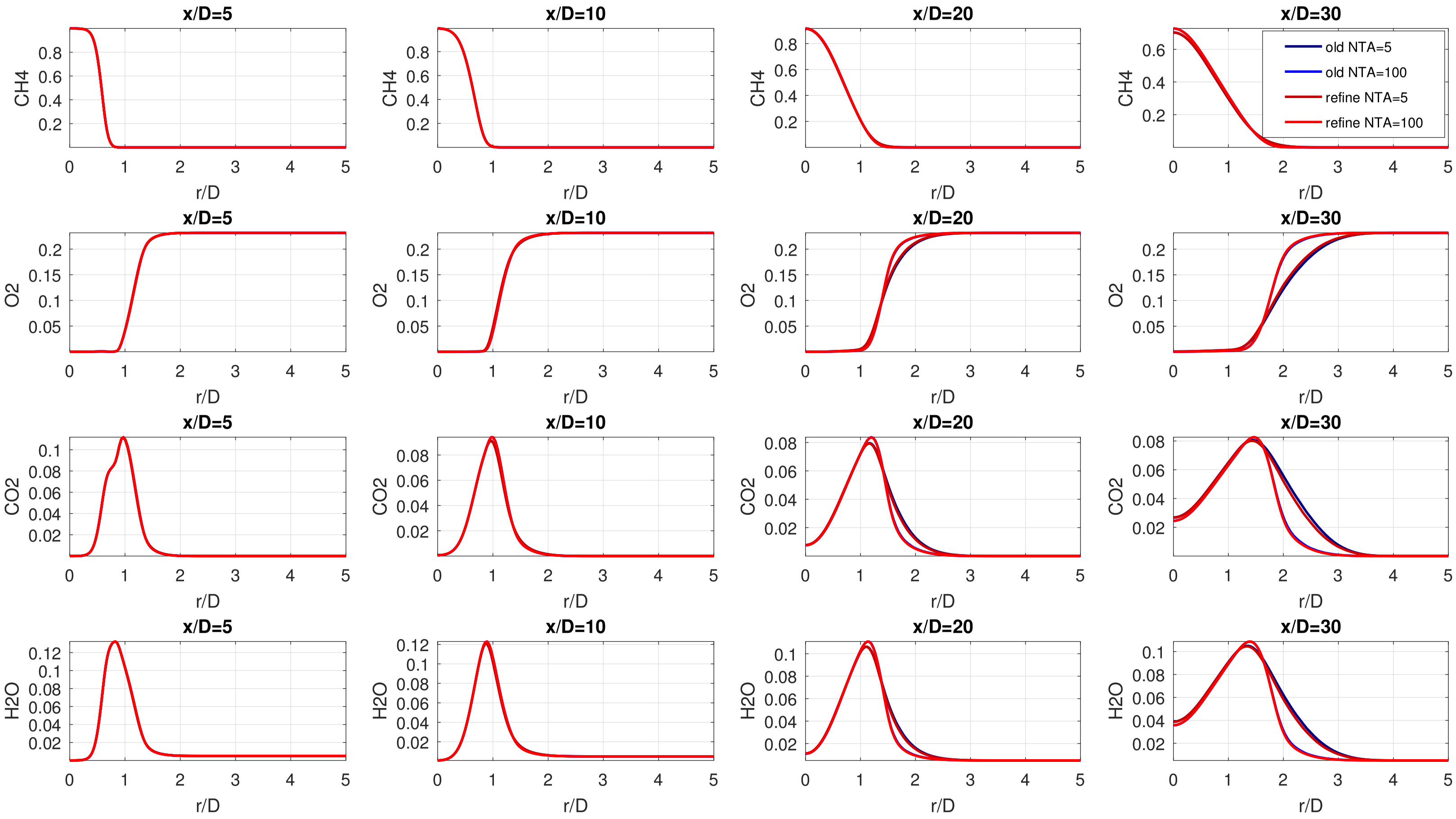

Figure 4.11. Radial profiles of CH_4, O_2, Co_2 and H_2O with NTA=5 and NTA=100 cases on both standard and refined grid.

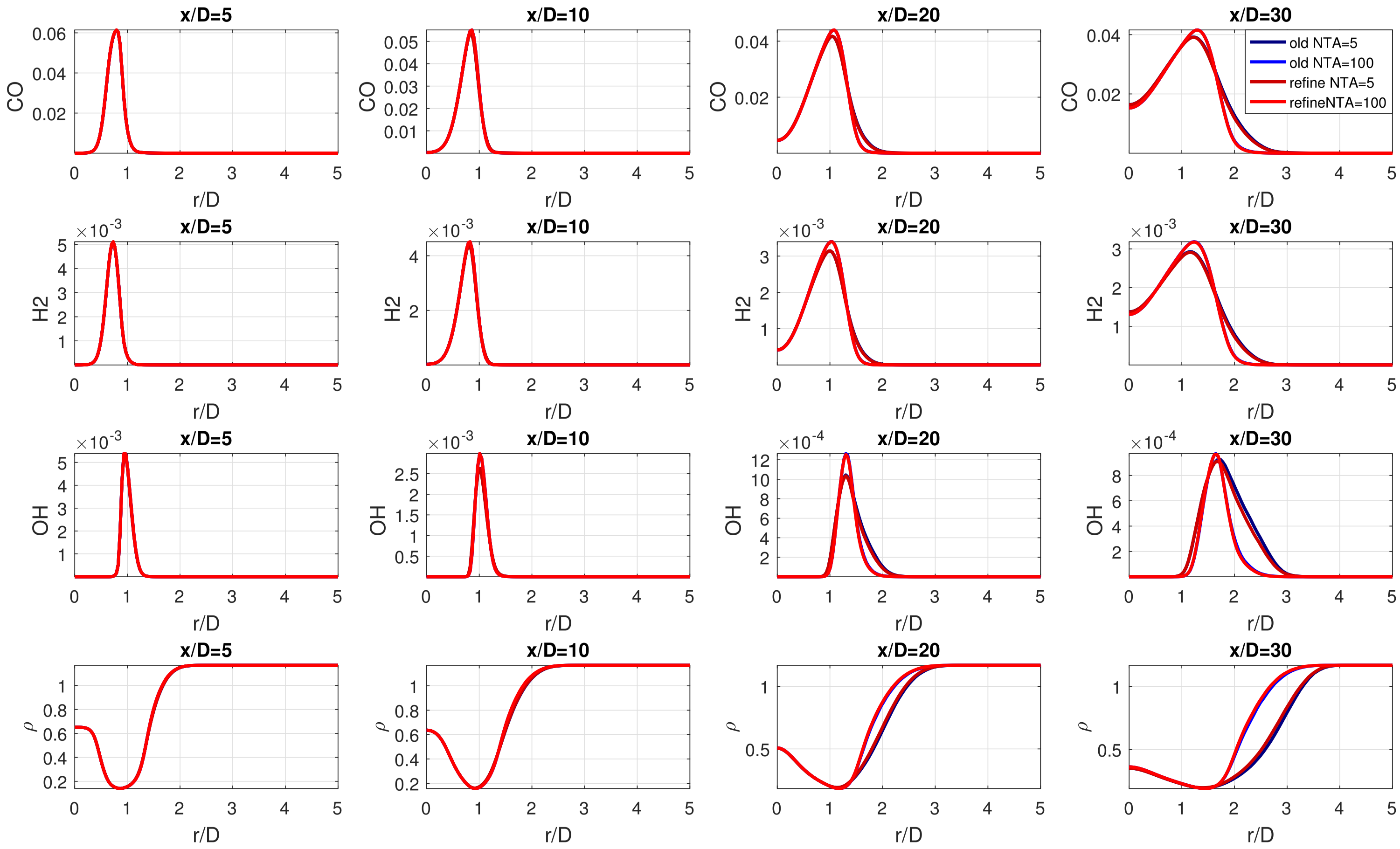

Figure 4.12. Radial profiles of CO, H_2, OH and ρ with NTA=5 and NTA=100 cases on both standard and refined grid.

4.2 Effect of Modeling Constants $C_{\epsilon 1}$ and Sc

Parametric studies of $C_{\epsilon 1}$ and Sc are usually conducted in flame studies to get correct peak magnitude, peak location and spreading of the flame. In this studies, these two parameters are also studied to ensure promising result for turbulent pulsed jet flame simulations.

4.2.1 Effect of Different $C_{\epsilon 1}$

$C_{\epsilon 1} = 1.44$ is the default value and is commonly used in other flow simulations that using RANS $k - \epsilon$ model. However, this default setting needs to be improved for predicting composition fields. Fig. 4.13-4.15 show radial profiles of cases with following $C_{\epsilon 1}$: 1.44, 1.50, 1.60, 1.70 and 1.80. Default value of $C_{\epsilon 1} = 1.44$ has good alignment with mean axial velocity U, but can not predict composition field correctly. By varying this coefficient, all test cases do have good alignment with the experimental data when close to exit plane. While moving to down stream, it is hard for a single test cases capture both velocity and composition fields of the flame correctly. Generally, test case with $C_{\epsilon 1} = 1.6$ have good performance in predicting flame shapes and composition fields. So $C_{\epsilon 1} = 1.6$ is chosen as the standard value for all the following calculations.

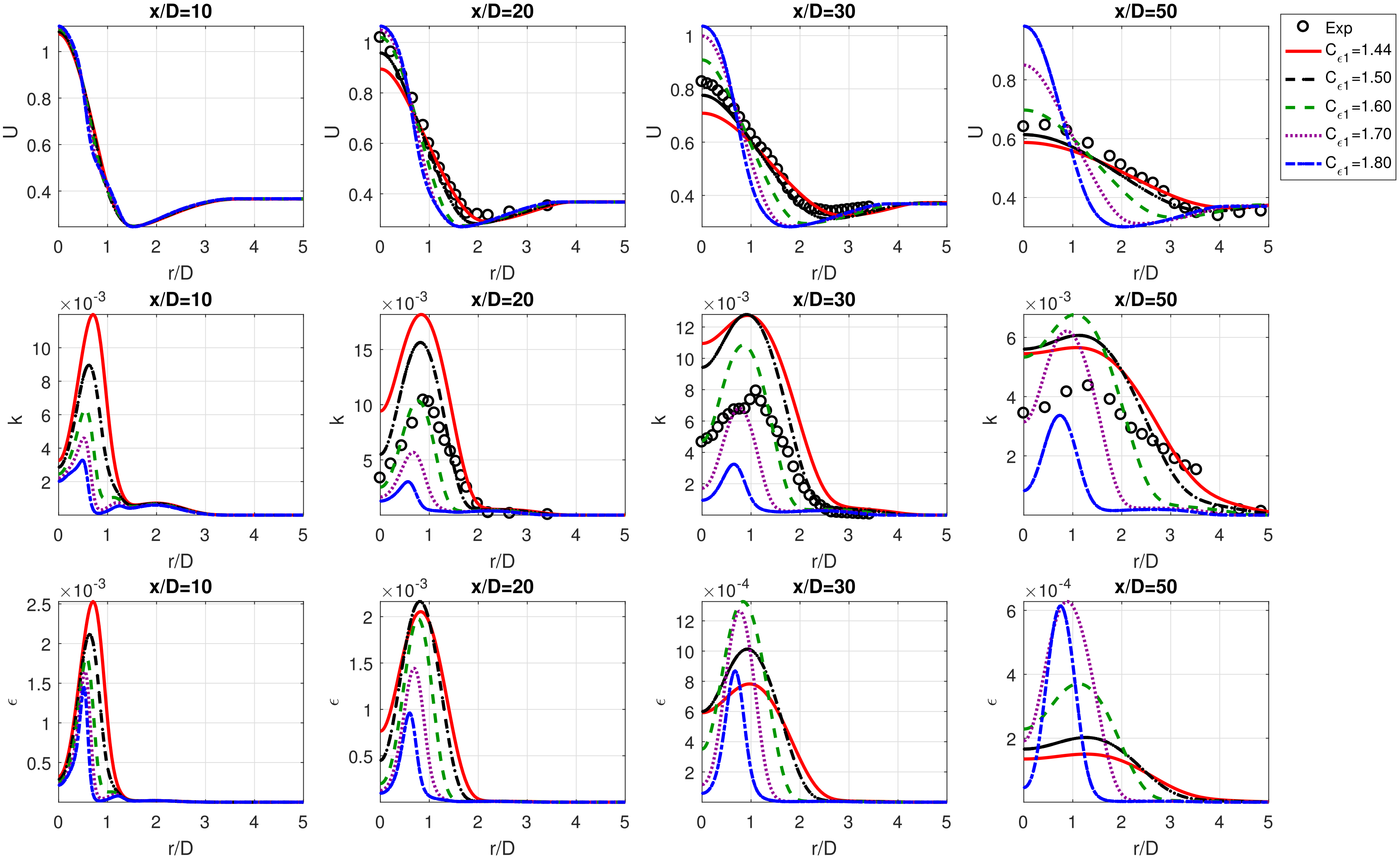

Figure 4.13. Radial profiles of mean axial velocity U, turbulent kinetic energy k and dissipation ϵ with different $C_{\epsilon 1}$ compare to experimental data.

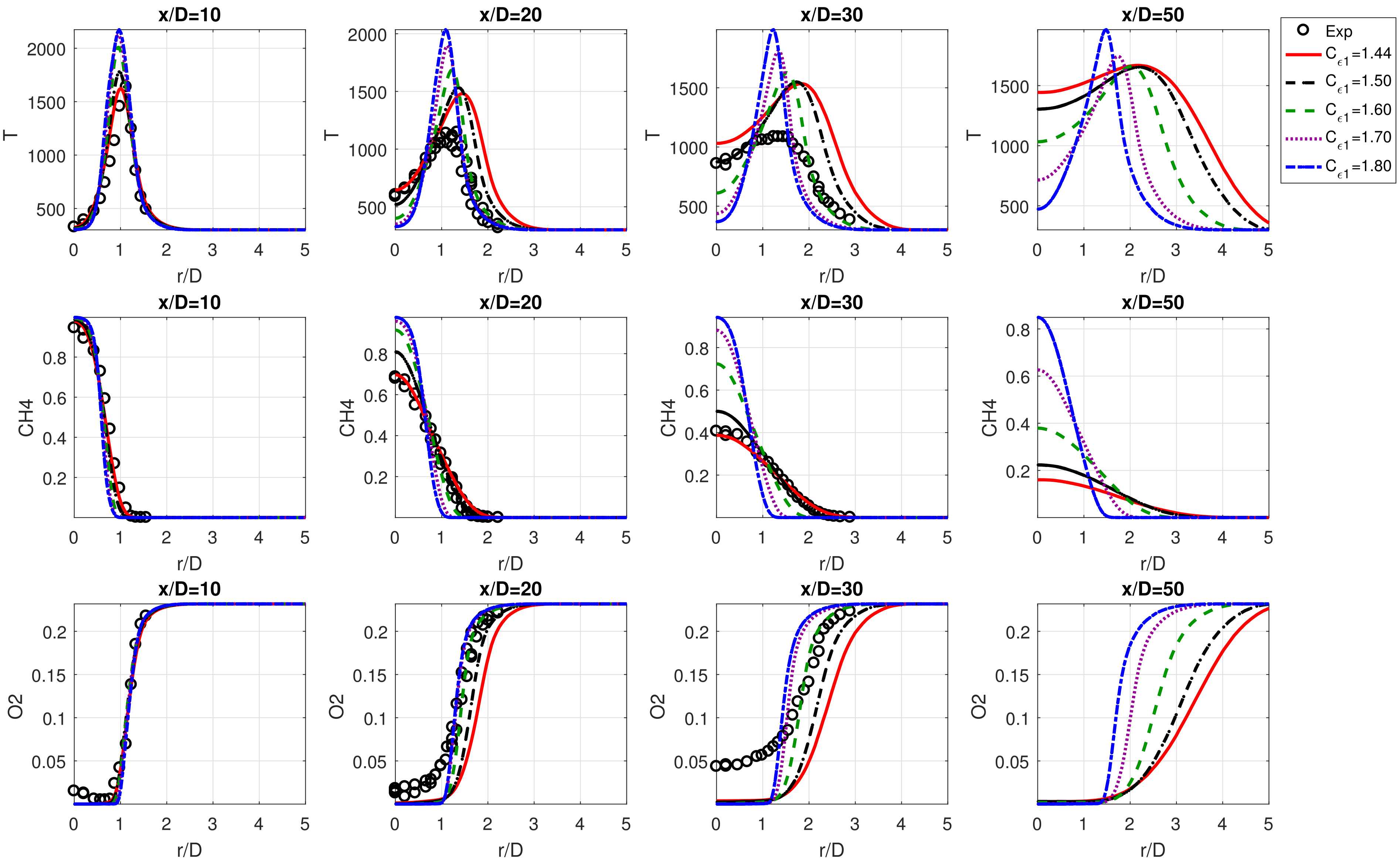

Figure 4.14. Radial profiles of mean temperature T, CH_4 and O_2 with different $C_{\epsilon 1}$ compare to experimental data.

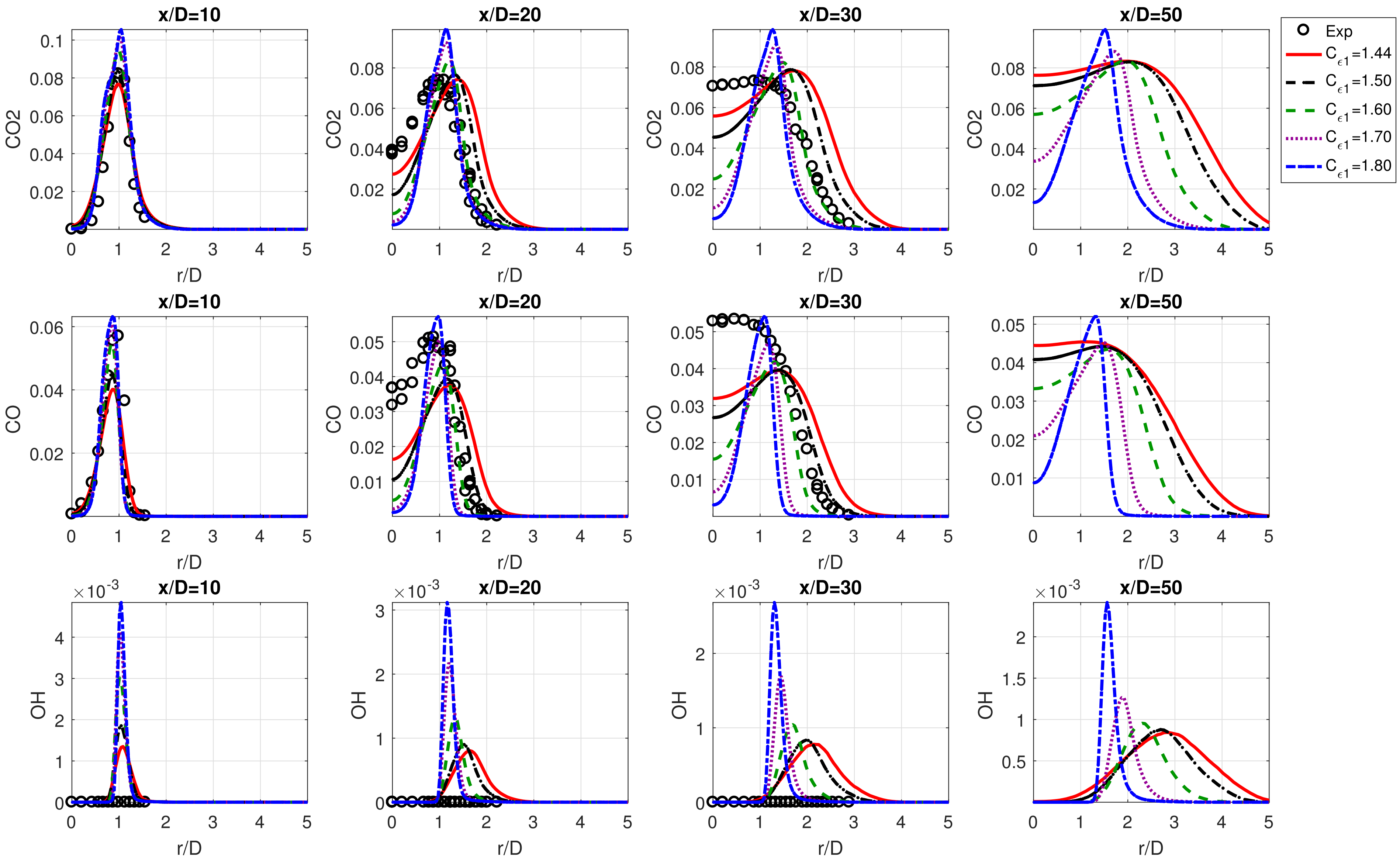

Figure 4.15. Radial profiles of CO_2, CO and H_2 with different $C_{\epsilon 1}$ compare to experimental data.

4.2.2 Effect of Different Sc

Schmidt number is another coefficient that usually been studied for a flame because it also affects spreading of a flame. Default value of 0.85 is commonly used in flame study with RANS models. Test cases with $Sc = 0.70$, 0.80, 0.85, 0.90 and 1.00 are tested with their results plotted in fig. 4.16-4.18. The obtained results show very little variation for schmidt number so original value of $Sc = 0.85$ is chosen to proceed.

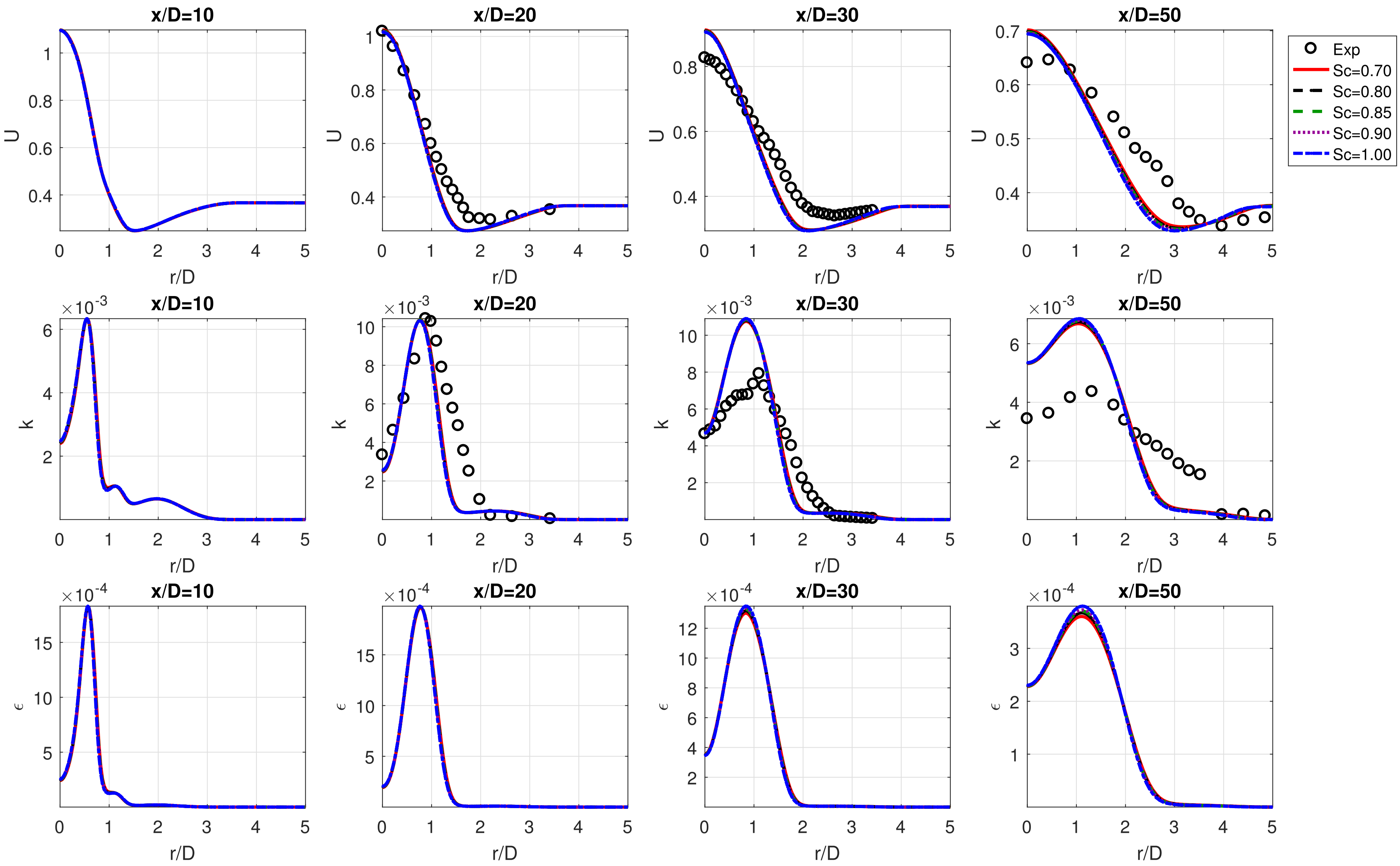

Figure 4.16. Radial profiles of mean axial velocity U, turbulent kinetic energy k and dissipation ϵ with different Sc compare to experimental data.

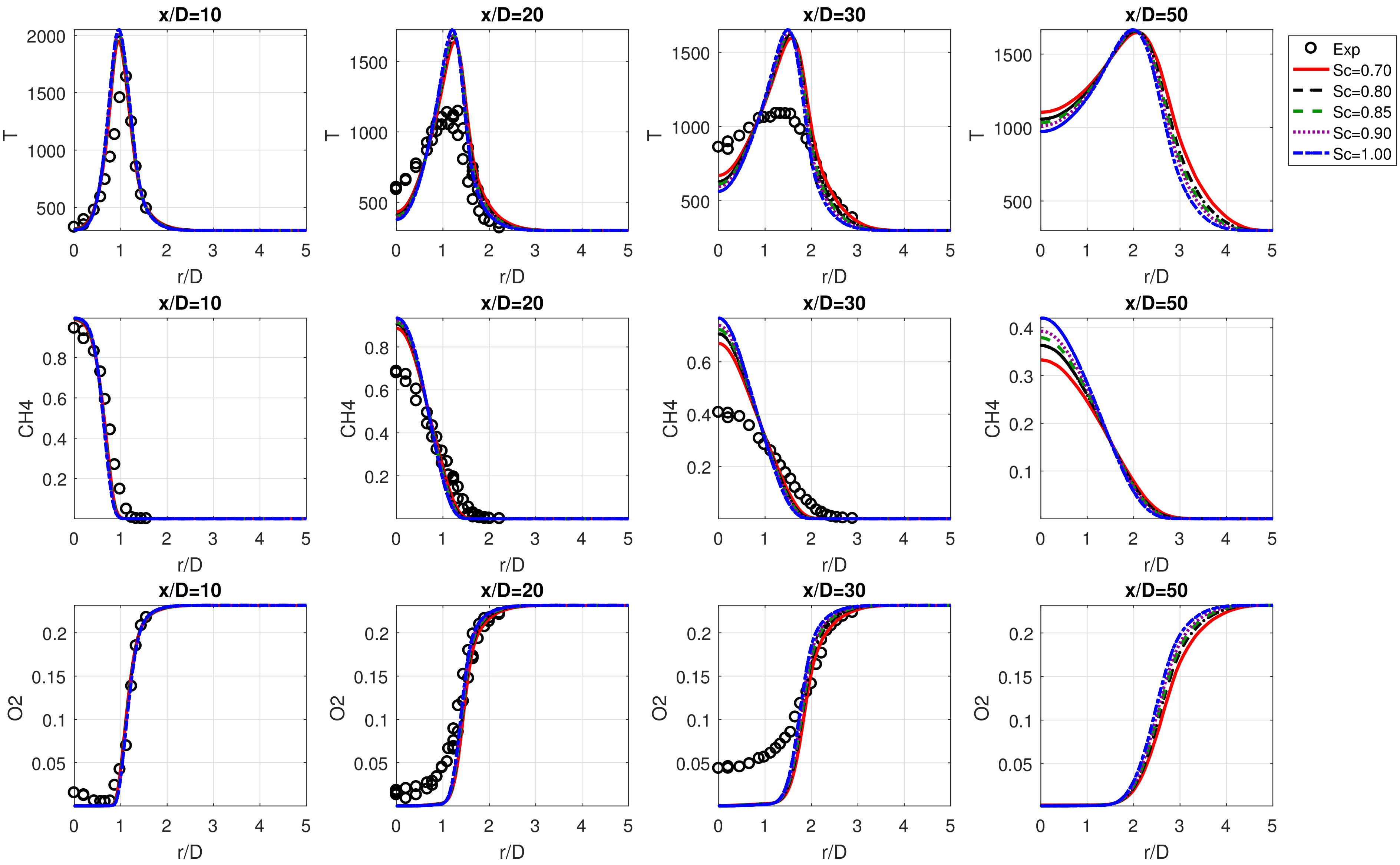

Figure 4.17. Radial profiles of mean temperature T, CH_4 and O_2 with different Sc compare to experimental data.

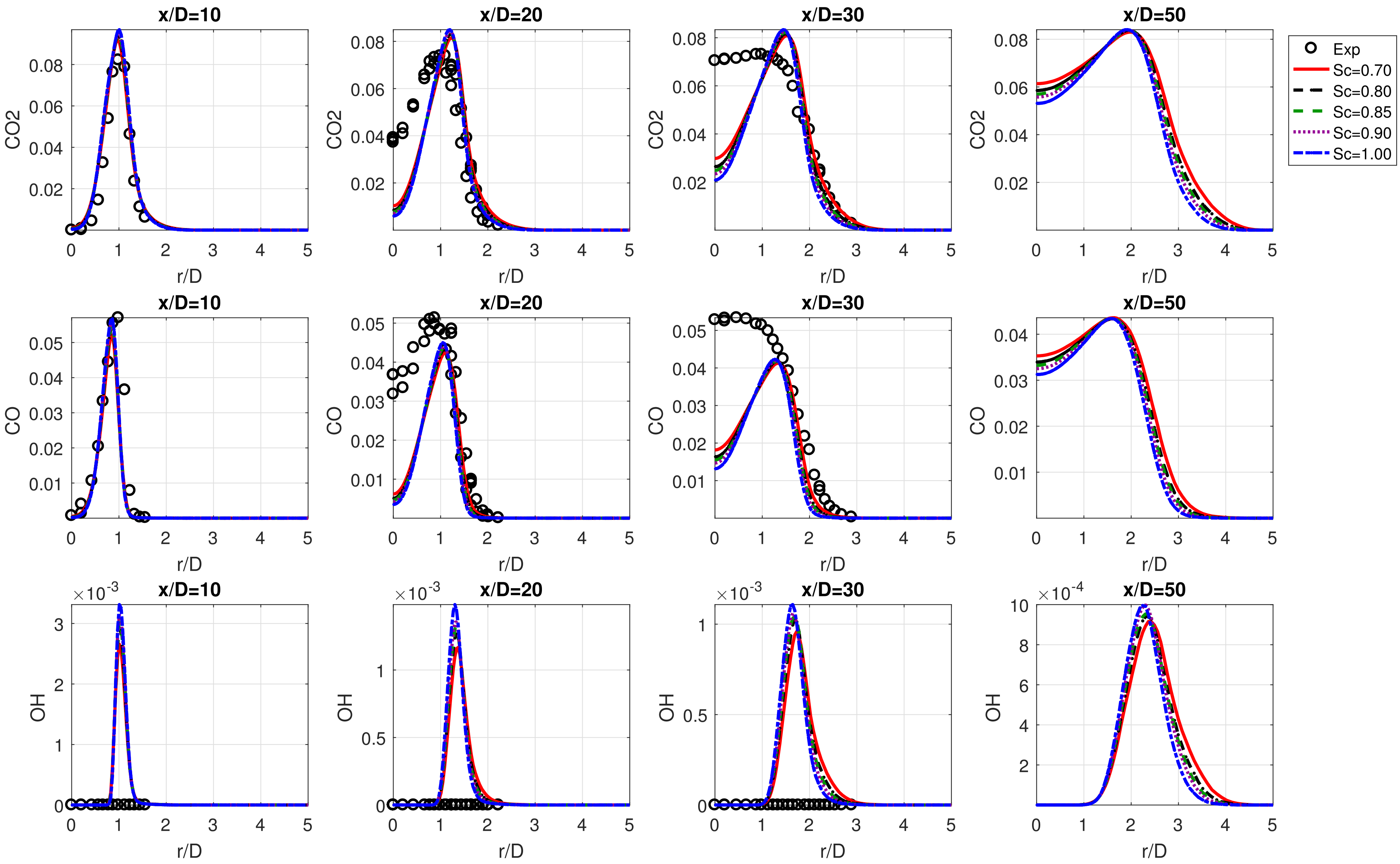

Figure 4.18. Radial profiles of CO_2, CO and H_2 with different Sc compare to experimental data.

4.3 Effect of Mixing Models and Mixing Coefficient C_ϕ

Mixing models and mixing coefficient C_ϕ affect variance profiles and capability of burning for a flame. Study performed in this section is to evaluate effect of mixing models and mixing coefficient on Flame L. and also to answer whether there exists a setup of mixing model and mixing coefficient C_ϕ that can solely represent Flame L and proceed to turbulent pulsed jet flame simulation.

4.3.1 IEM Mixing Model

IEM mixing model with mixing coefficient C_ϕ=2, 4, 6 and 8 are tested with results presented in fig. 4.19-4.21. As shown in radial profile of temperature T, CO and CO_2, increasing mixing coefficient enhance burning in the flame. Experimental data of OH radicals are not available here, but since OH radical can reflect how much reaction is taken place, radial profiles of OH from simulation are presented for all three mixing models. Radial profiles for outer region of the flame from experimental data is more close to cases with C_ϕ=6 and 8. Also, OH profiles have much larger magnitude for those C_ϕ values. Thus, cases with $C_\phi = 6$ and above are considered as burning flame.

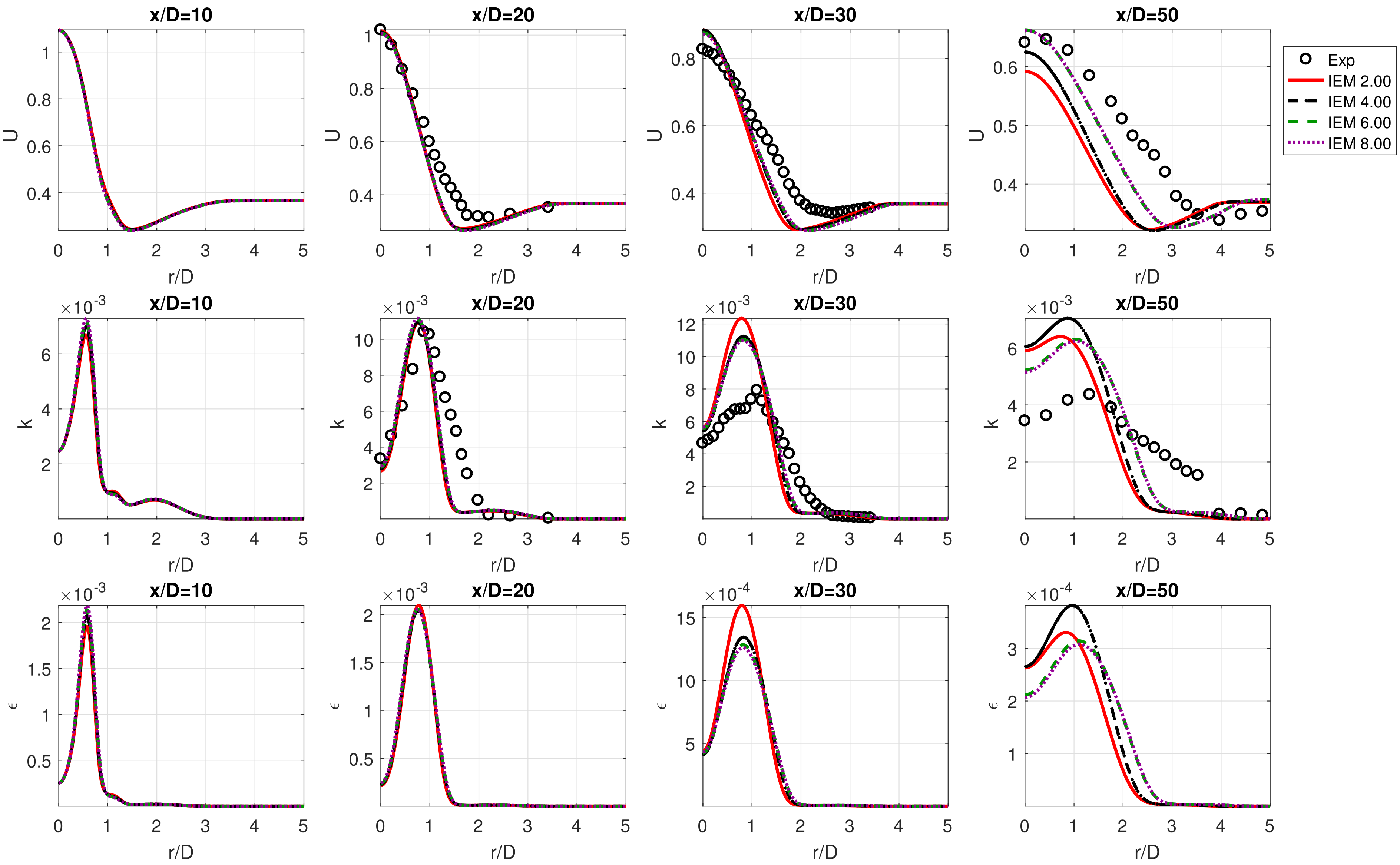

Figure 4.19. Radial profiles of mean axial velocity U, turbulent kinetic energy k and dissipation ϵ of IEM mixing models compare to experimental data.

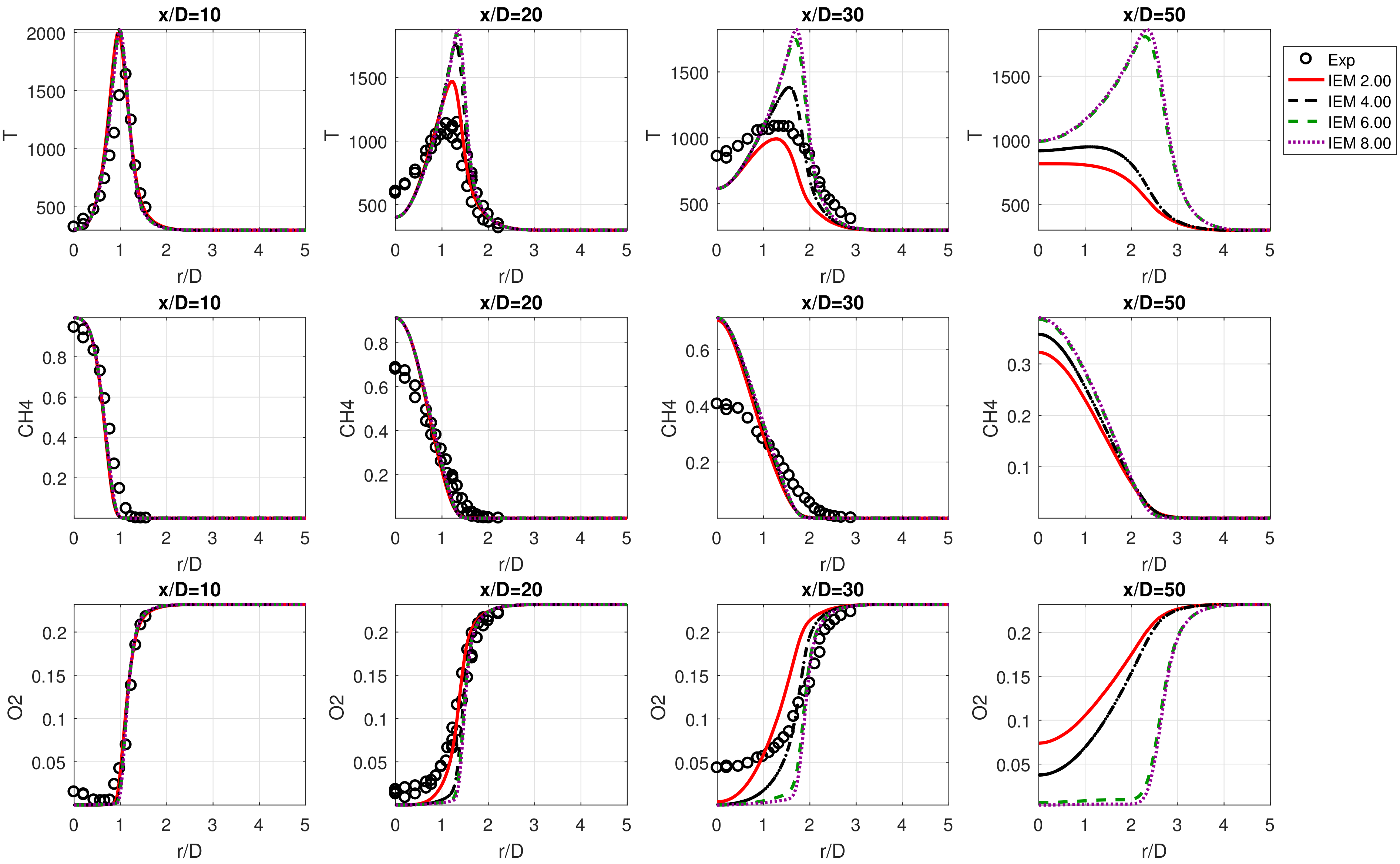

Figure 4.20. Radial profiles of mean temperature T, CH_4 and O_2 of IEM mixing models compare to experimental data.

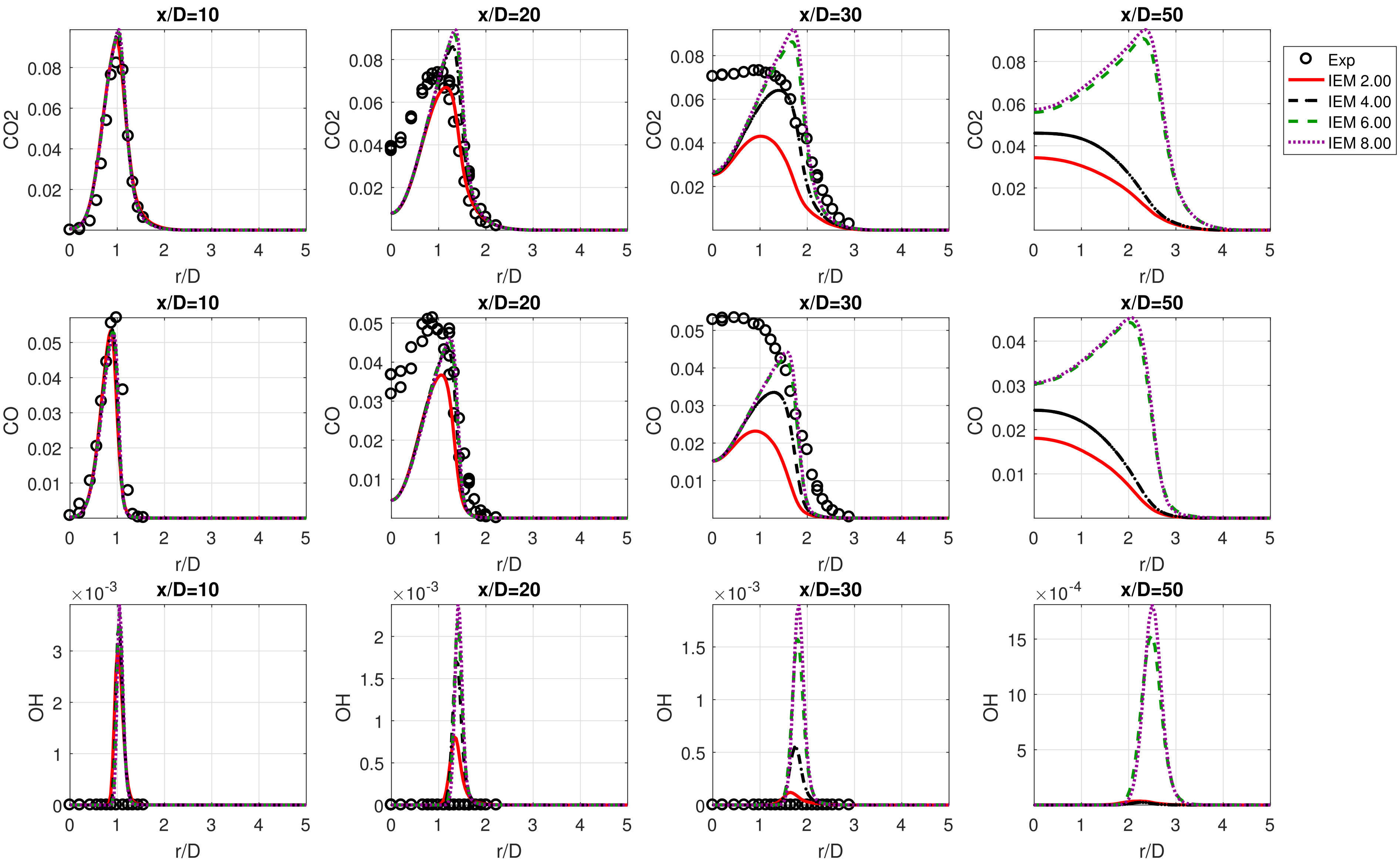

Figure 4.21. Radial profiles of CO_2, CO and OH of IEM mixing models compare to experimental data.

4.3.2 MCurl Mixing Model

Modified Curl mixing model adds more localness when comparing to IEM mixing model. Thus, with the same mixing coefficient C_ϕ, case with MCurl mixing model has more burning when comparing to case with IEM mixing model. Overall profiles of MCurl mixing model are similar to IEM model. As C_ϕ increasing, more reaction is presented, and simulation results moves from not burning to burning. From radial profiles of O_2, CO_2, CO and OH in fig. 4.22-4.24, one can tell that MCurl mixing model with mixing coefficient $C_\phi = 4$ and above can produce a burning flame.

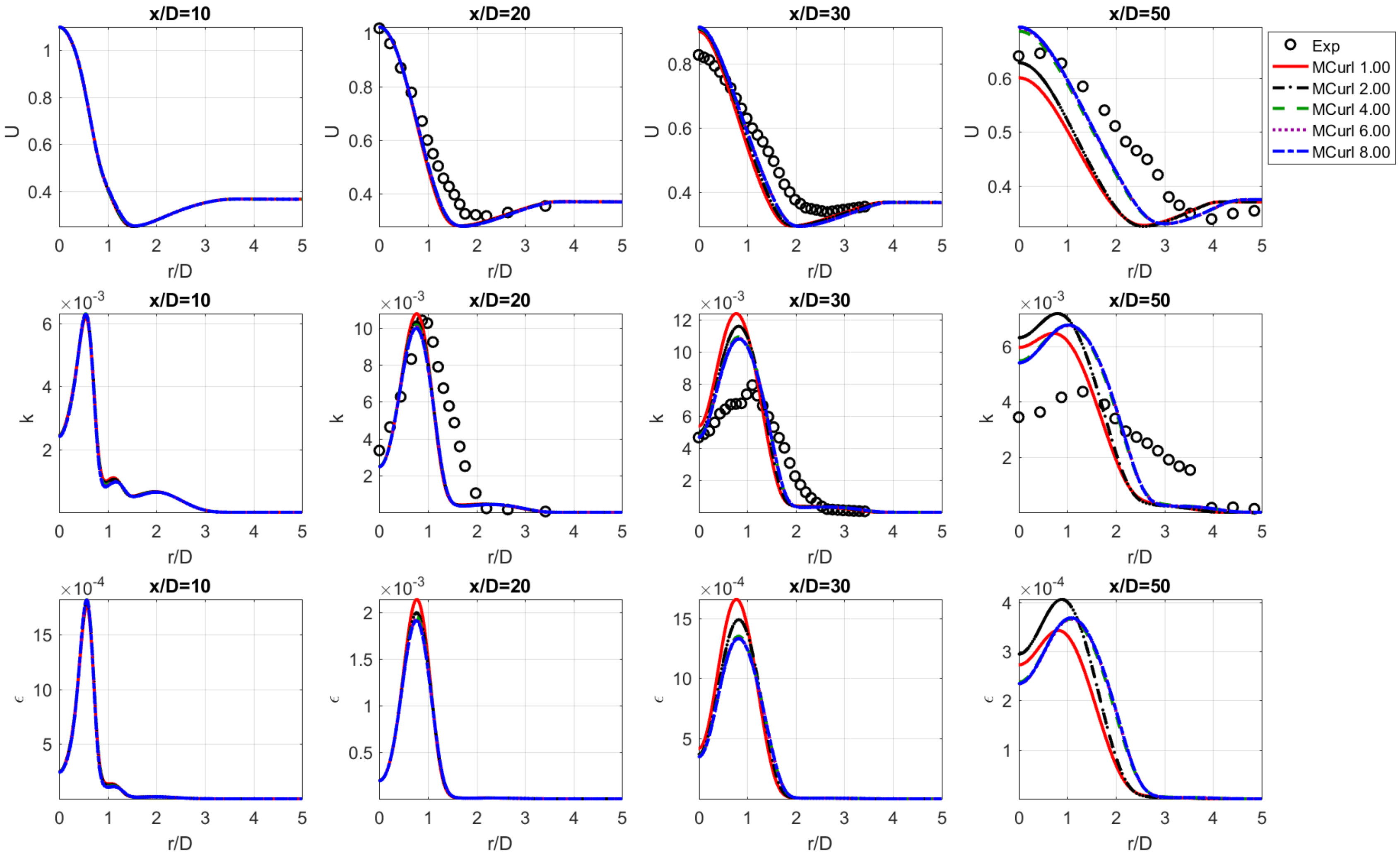

Figure 4.22. Radial profiles of mean axial velocity U, turbulent kinetic energy k and dissipation ϵ of MCurl mixing models compare to experimental data.

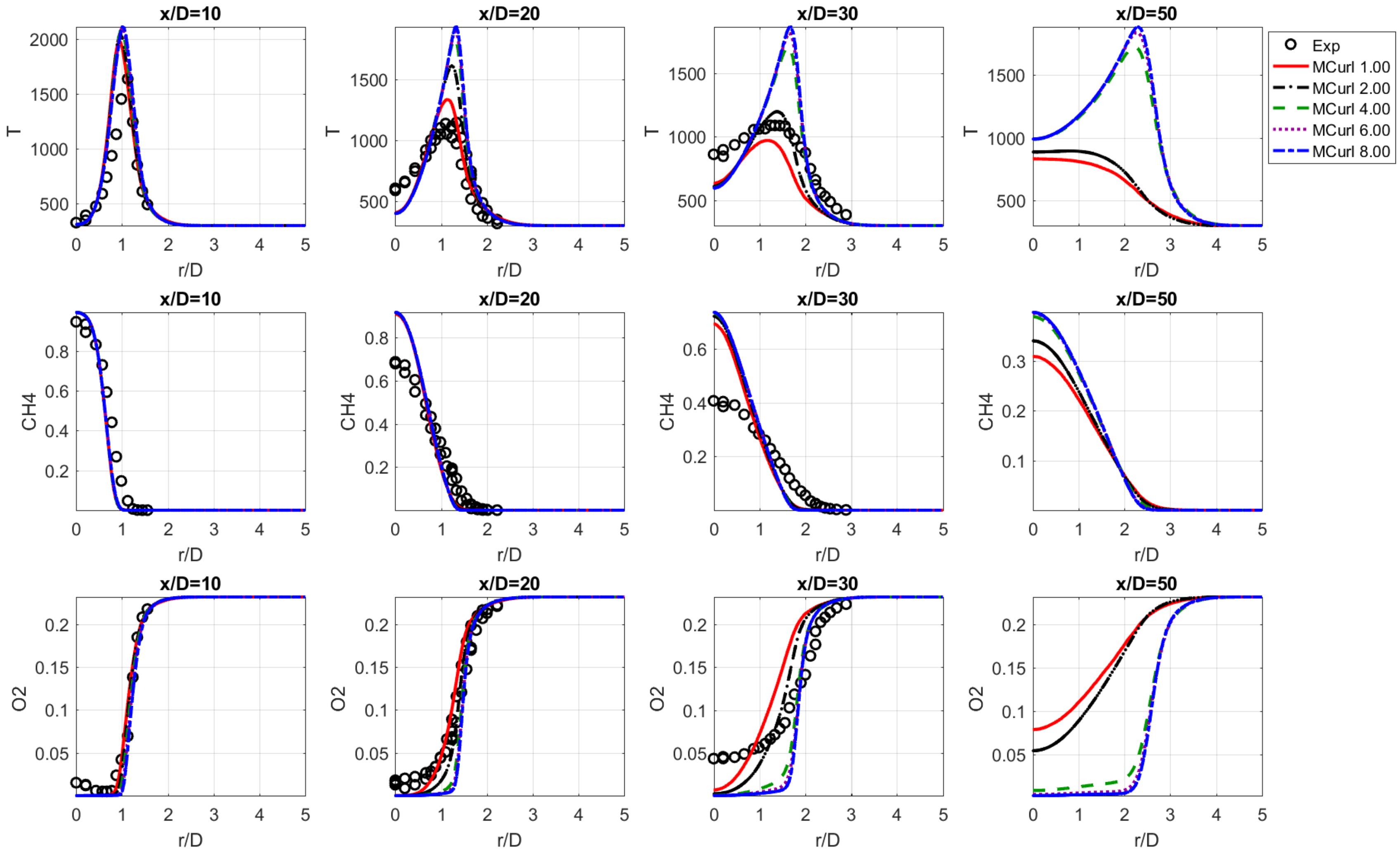

Figure 4.23. Radial profiles of mean temperature T, CH_4 and O_2 of MCurl mixing models compare to experimental data.

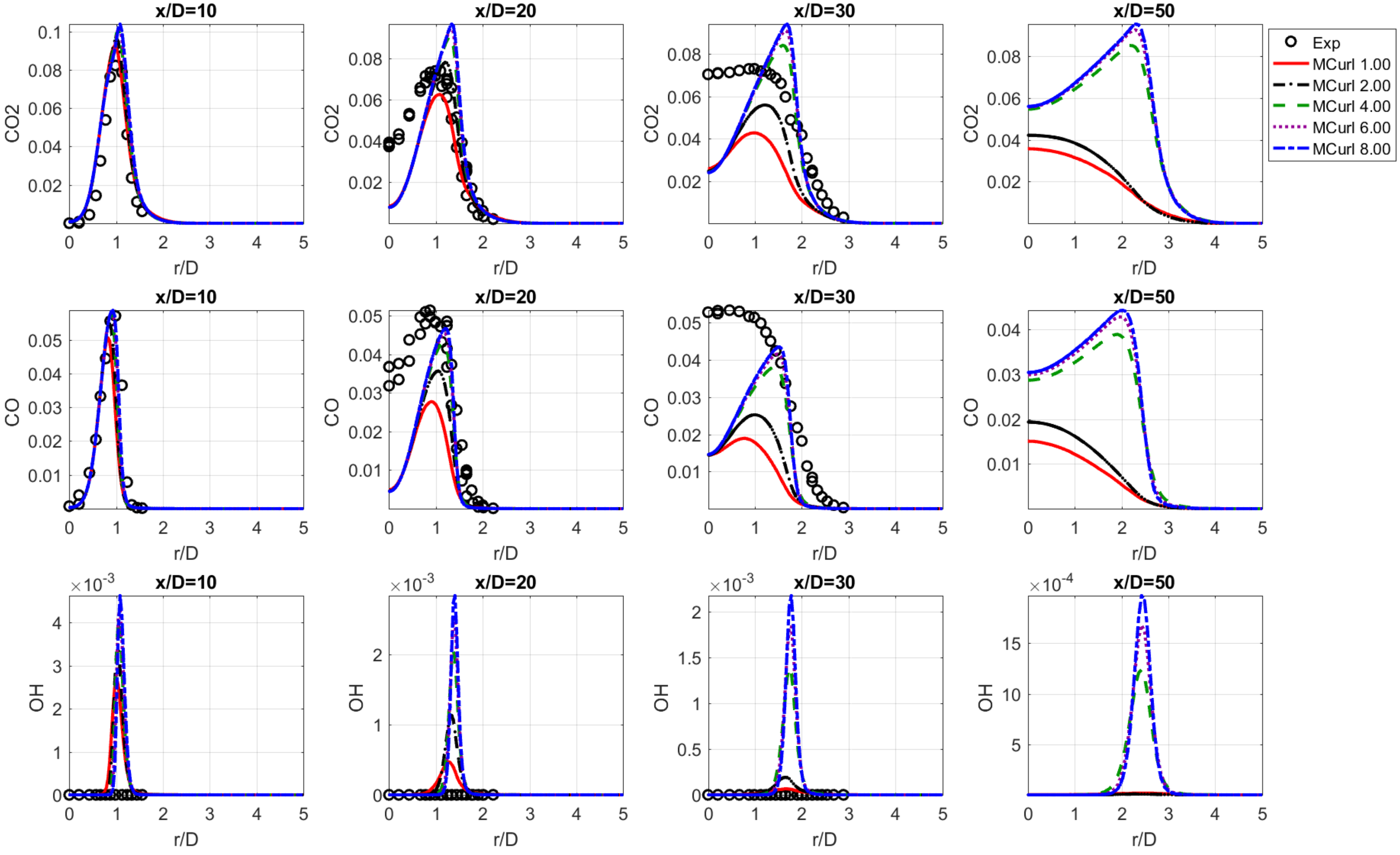

Figure 4.24. Radial profiles of CO_2, CO and OH of MCurl mixing models compare to experimental data.

4.3.3 EMST Mixing Model

Unlike results with IEM and MCurl mixing model, results with EMST mixing model merely changes when mixing coefficient C_ϕ varies, as shown in fig. 4.25-4.27. Results with EMST mixing model always show as a burning flame no matter how small the mixing coefficient C_ϕ is. Radial profiles of OH radicals have significant spreading phenomenon as C_ϕ decreases, which can also be observed in section 5.1 in OH contour plots.

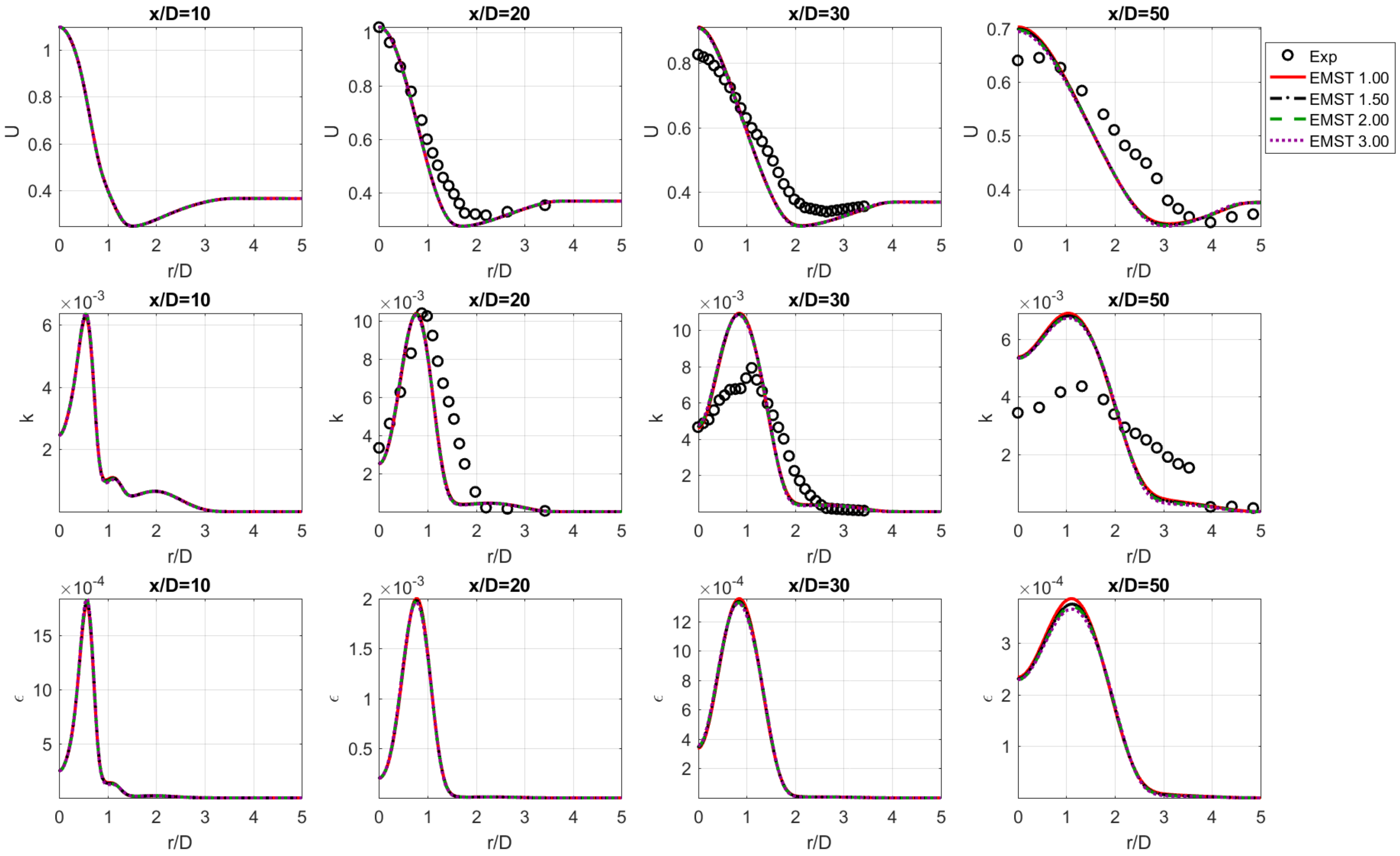

Figure 4.25. Radial profiles of mean axial velocity U, turbulent kinetic energy k and dissipation ϵ of EMST mixing models compare to experimental data.

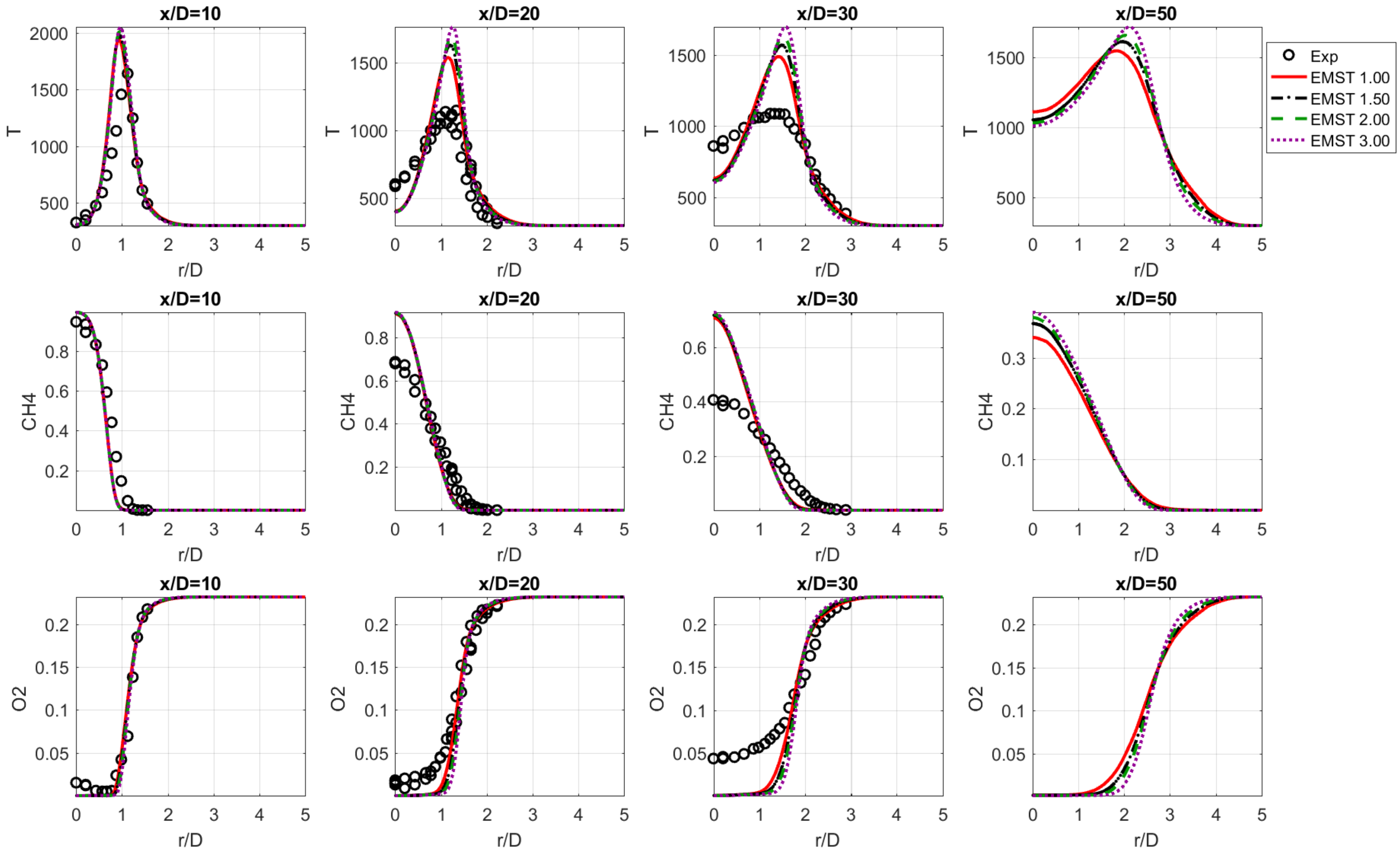

Figure 4.26. Radial profiles of mean temperature T, CH_4 and O_2 of EMST mixing models compare to experimental data.

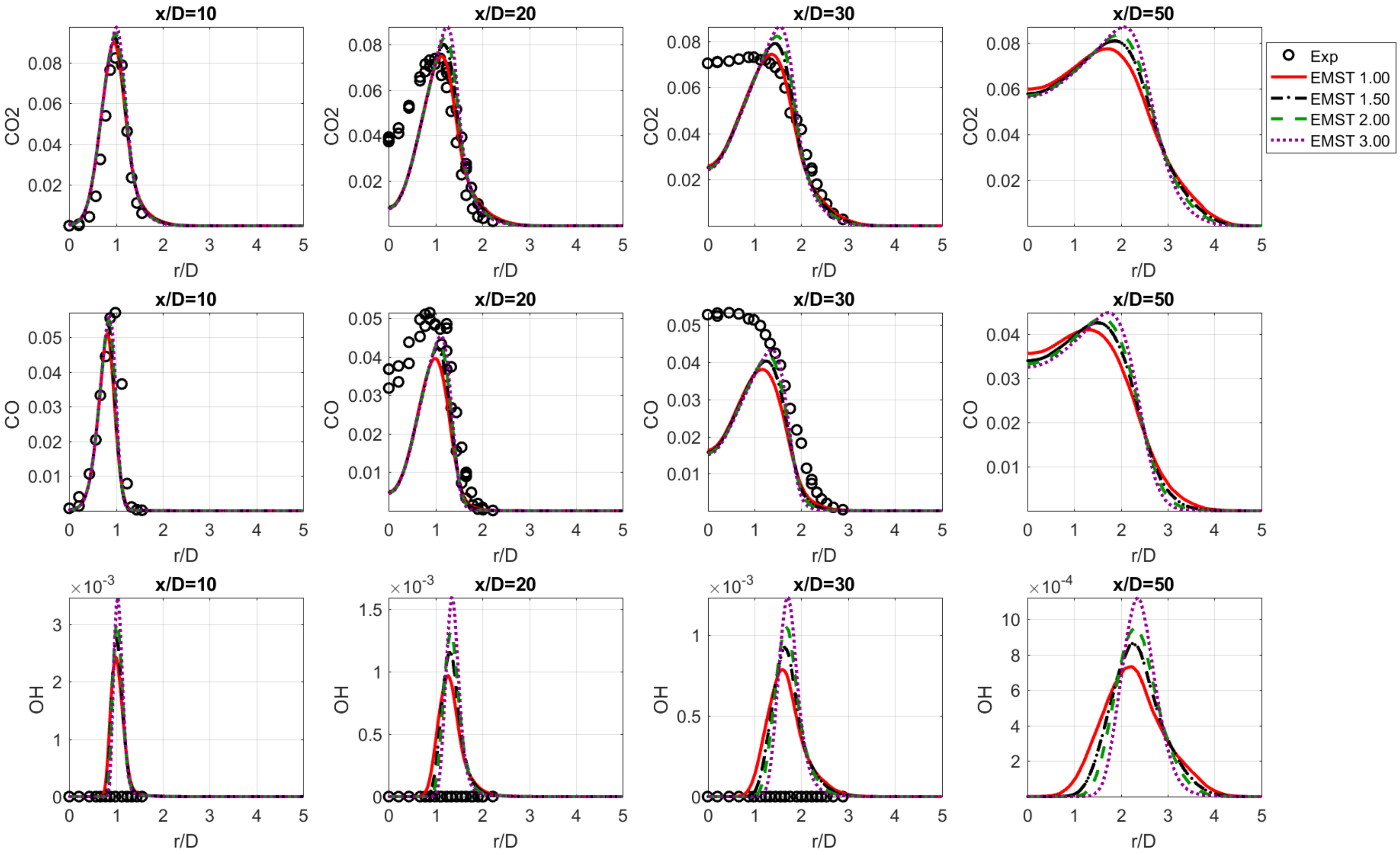

Figure 4.27. Radial profiles of CO_2, CO and OH EMST mixing models compare to experimental data.

4.4 Effect of Particle Number, NTA on simulation accuracy

Since PDF method with particle method are implemented for solving composition fields, number of particles (N_{pc}) also affects accuracy of simulation results. More particles give more accurate results. However, increasing number of particles will also increase computational cost linearly for mixing subroutine. For IEM and MCurl mixing model, $t \sim N_{pc}$ since number of calculations required for mixing, reaction, transporting are proportional to particle number. As for EMST mixing model, since distance between each particle in composition space needs to be calculated, and also based on test data provided in table 4.1, second order linear relation can be generated for N_{pc} and time. Thus, $t \sim N_{pc}^2$ for cases with ESMT mixing model.

Table 4.1. Time required for a 20 steps calculation with EMST mixing model

N_{pc}	100	200	400	600
Total simulation time(s)	154.59	217.65	736.26	1911
Moderate mixing time per step(s)	0.8-1.2	1.6-2.3	5.5-10	10.7-20
Longest mixing time per step(s)	4.8	9.4	37	98

Based on the above N_{pc}-time relation, appropriate value of N_{pc} is desired so that one can perform simulation accurately with an acceptable computational cost. Since moving time averaging (MTA) technique is applied in this study, particles from a period of time steps all contribute to finding the accurate solution, and effective particle number($N_{pc,eff}$) is defined as the following:

$$N_{pc,eff} = N_{pc} \times NTA. \tag{4.2}$$

A series of test cases with different particle number is tested with $NTA = 100$, the effective particle number ($N_{pc,eff}$) for those cases are: 500, 800, 1000, 1100, 1400, 1700, 2000, 2500, 3000, 4000, 5000, 10000. Part of the results is shown in fig. 4.28,

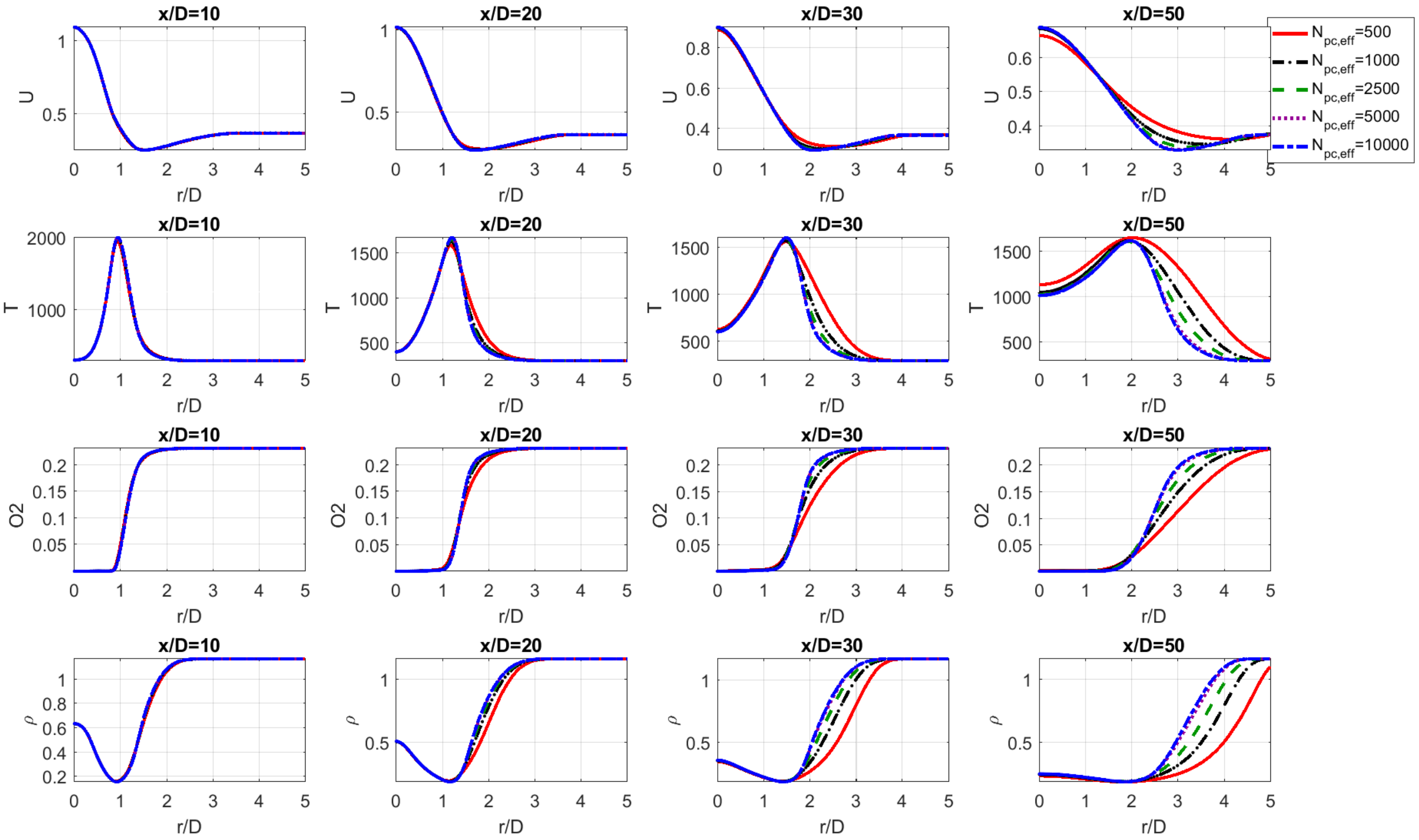

Figure 4.28. Radial profiles of different $N_{pc,eff}$ for selected variables.

and large variations is observed in region $r/D > 2$ although almost no difference are found inside the flame. Since this grid spacing arrangement passed the convergence test, grid resolution shall not be problem here. A concern regarding dramatically changing in grid size was raised. A following grid refinement study is performed in section 4.1.2 and proved that grid has no effect on this variation. Thus, this variation is caused by varying $N_{pc,eff}$.

Scatter plots of selected locations are shown in fig. 4.29-4.31, and only mean axial velocity U, mean temperature T and mean fuel mixture fraction ξ are shown here. Values are plotted against inverse of $N_{pc,eff}$ to show converging trend. Solid lines in each plot are the fitted first order function for all points. The intersection of fitted line and vertical axis represents as solution with infinite number of particles, which should contain no random error from particle method. Blue dotted lines and red dashed lines are relative errors calculated using eq. 4.1, where ϕ_{target} here uses solution with infinite number of particles. Blue dotted lines represent ±1% relative error and red dashed lines represent ±5% relative error. Locations where values$\leq 1 \times 10^{-3}$ are not considered. After analyzing all quantities, it is concluded that $N_{pc,eff} = 3000$ is required to have errors smaller than 5%.

The following constrains are obtained for N_{pc}, NTA and dt:

$$dt \times NTA \ll 3.01 \times 10^{-4} s,\ from\ section\ 2.2.2, \tag{4.3}$$

$$N_{pc} \times NTA \geq 3000. \tag{4.4}$$

Previous simulations were run using a non-dimensional time of 0.015, which is $2.63415 \times 10^{-6} s$ before normalized by fuel tube diameter and fuel tube bulk velocity:

$$dt_{old} \frac{U_{bulk}}{D} = 2.63415 \times 10^{-6}(s) \frac{41(m/s)}{7.2 \times 10^{-3}(m)} = 0.015. \tag{4.5}$$

Pulse time scale constrain of $3.01 \times 10^{-4} s$ is about 114 dt_{old}. Since much smaller scale is desired, 10 dt_{old} is obtained after square root, which is $2.63415 \times 10^{-5} s$. And the relation of dt, NTA can be narrow to:

$$dt \times NTA = 2.63415 \times 10^{-5} s \tag{4.6}$$

Due to second order increasing in computational cost of N_{pc} for EMST mixing model, maximum particle number cannot exceed 100. With information provided above, dt, NTA and N_{pc} are decided as following: $N_{pc} = 100$, $NTA = 30$ and $dt = 8.7805 \times 10^{-7}(s)$ or 0.005 for turbulent pulsed jet flame.

With the above studies presented, an optimal setting is generated for turbulent pulsed jet flame simulation except mixing models and mixing coefficients. Since mixing models and mixing coefficient also affect extinction gap in turbulent pulsed jet flame, mixing will continue to be studies in Chapter 5.

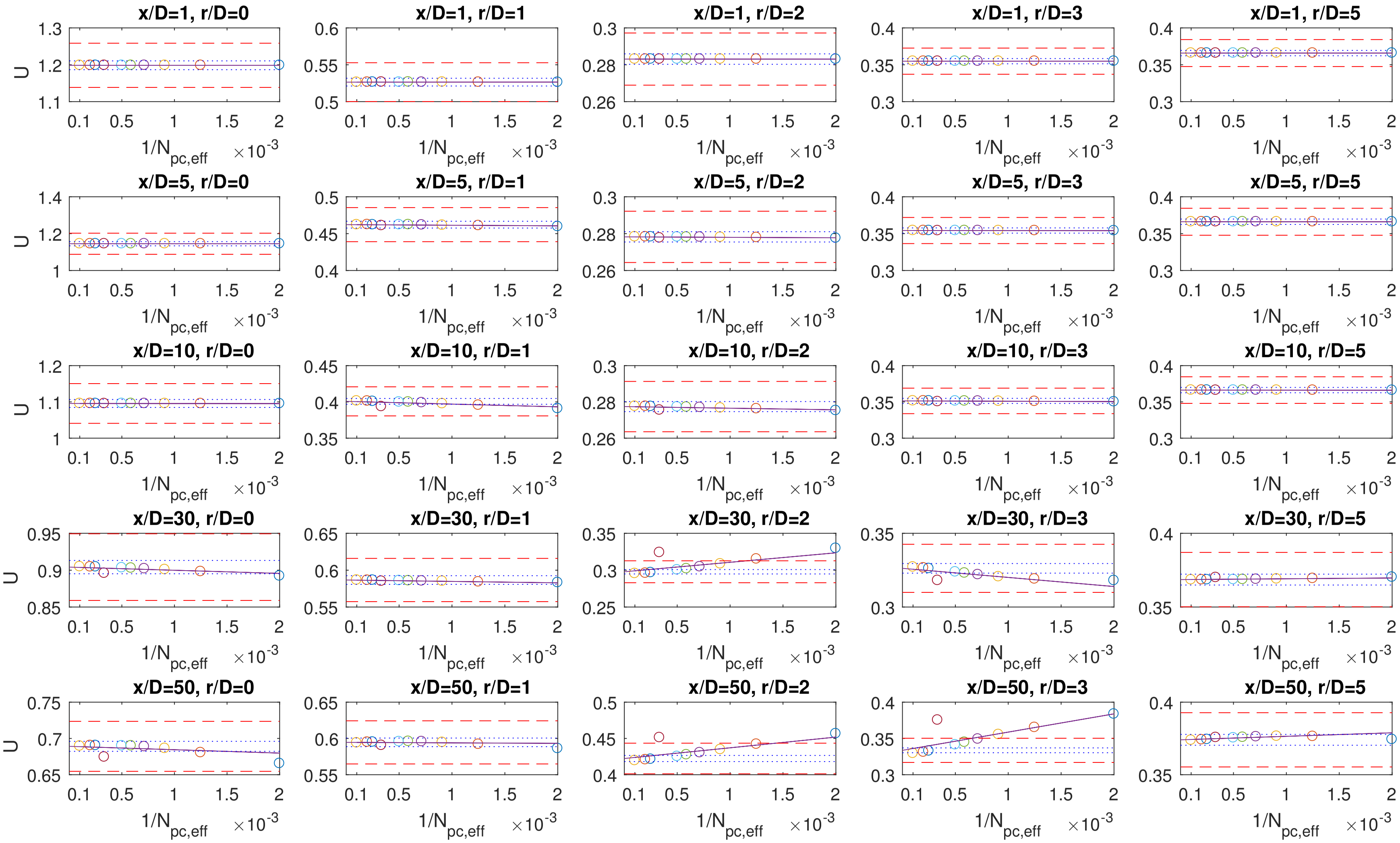

Figure 4.29. Scatter plots of mean axial velocity U for cases with different effective particle number at selected locations. Blue dotted lines represent 1% relative error and red dashed lines represent 5% relative error.

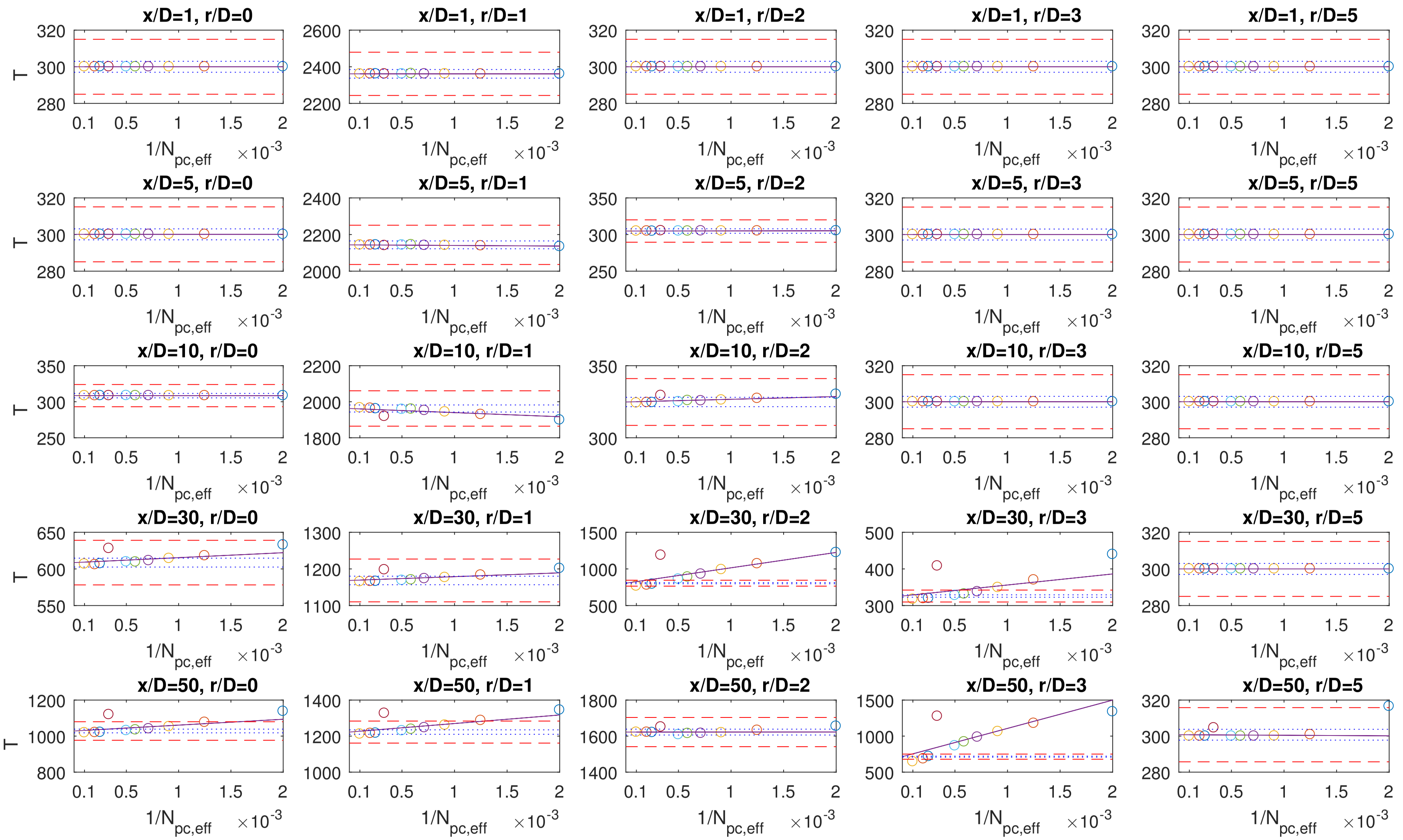

Figure 4.30. Scatter plots of mean temperature T for cases with different effective particle number at selected locations. Blue dotted lines represent 1% relative error and red dashed lines represent 5% relative error.

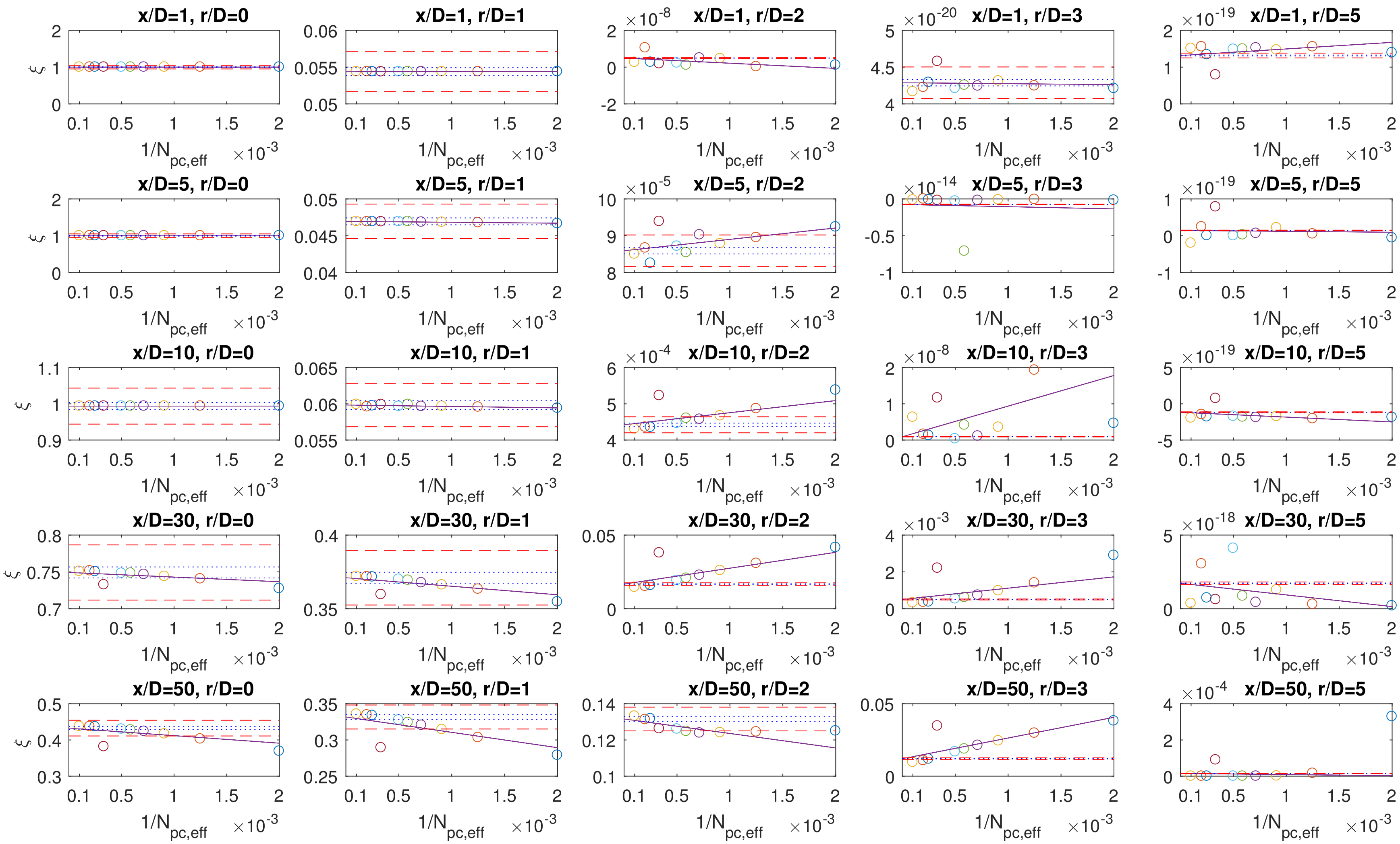

Figure 4.31. Scatter plots of mean fuel mixture fraction ξ for cases with different effective particle number at selected locations. Blue dotted lines represent 1% relative error and red dashed lines represent 5% relative error.

5. TURBULENT PULSED JET FLAME SIMULATION RESULTS AND DISCUSSION

Based on the parametric studies in Chapter 4, an optimal setting of coefficients can be used to perform simulations of turbulent pulsed jet flame with good accuracy and moderate computational cost. Since mixing model affects burning, extinction and re-ignition, multiple cases with different mixing model and mixing coefficients are calculated. Table 5.1 below shows cases with different mixing models and mixing coefficients C_ϕ for turbulent pulsed jet flame simulations.

Table 5.1. Turbulent pulse jet flame simulations with different mixing models and mixing coefficients

Model	Model Coefficient							
IEM	3.00	3.50	4.00	5.00	5.50	6.00	7.00	8.00
MCurl	3.00	3.50	4.00	5.00	5.50	6.00	7.00	8.00
EMST	0.50	1.00	1.50	2.00				

5.1 Effect of Mixing Model and Model Coefficient C_ϕ on Extinction Gap

In this section, effect of mixing model and mixing coefficient C_ϕ on extinction gap will be discussed along with a qualitative comparison of extinction gap location histories between experimental data and simulation results. Fig. 5.1 shows the pulse function that used to change fuel tube inlet profile. Actual pulse starts at $t = 10ms$, reaches its maximum at $t = 13ms$ and its minimum at $t = 26.5ms$. In experiments, it is observed that extinction starts to occur at $t = 15ms$, reaches full extinction at

$t = 18ms$ and back to burning normally at $t = 29ms$. Since only one realization of experimental video is available, comparison of ensemble averaged experimental video to simulation animation could not be presented.

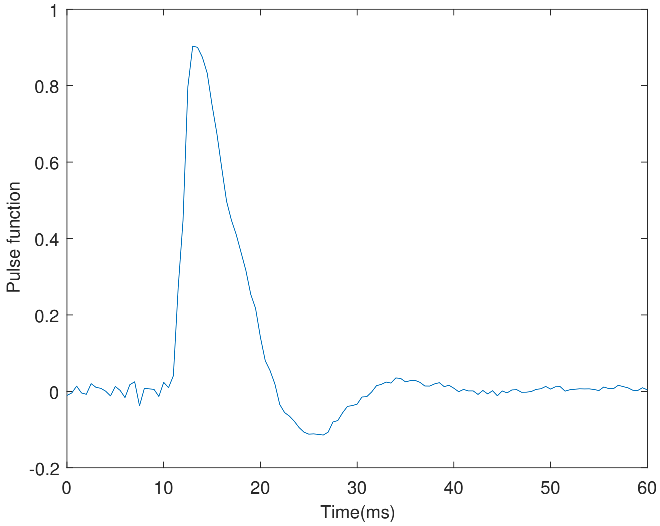

Figure 5.1. Pulse function used in simulation. Pulse starts at t=10ms.

Fig. 5.2 shows a series of contour plots that can represent a time history of the fields that using IEM mixing model with $C_\phi = 6$. Top row shows contours of mean axial velocity U, middle row shows temperature and plots in bottom row are OH radicals mass fraction contour. OH radicals are presented here since they are highly reactive and can be treated as a sign for reaction. For mean axial velocity, a high velocity region is present after pulse started. Then, this high velocity region is averaged out quickly without much information left in velocity contour plots. For temperature, a radial expansion of low temperature region inside the flame move towards down stream and break the flame to form an extinction gap with low temperature. With continuing flow supply, the gap also move towards downstream and exits the computational domain. For OH radicals mass fraction, reaction strip breaks when pulse function passed its peak and decreasing and form a dark region with negligible

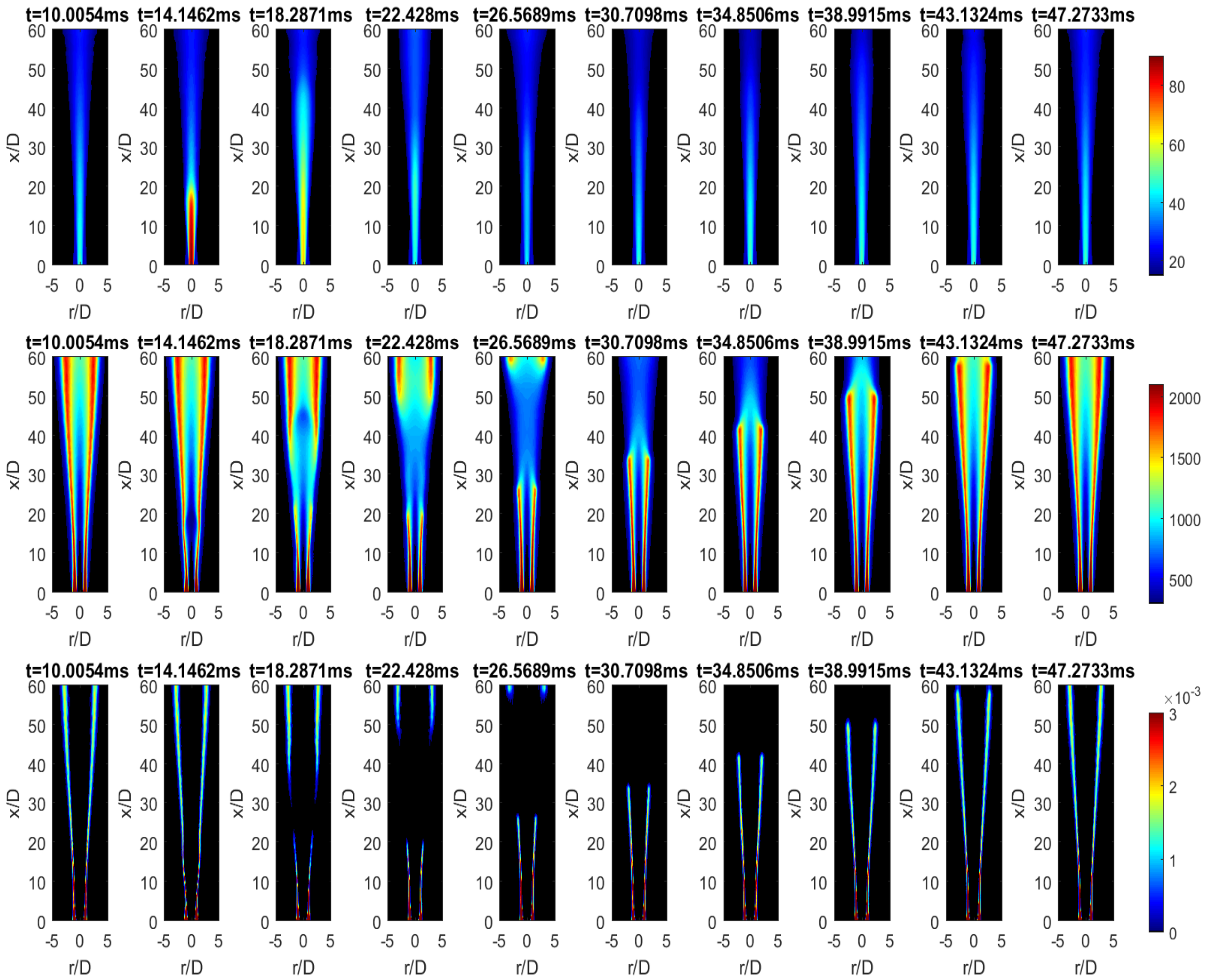

Figure 5.2. Contour plots of mean axial velocity U(top), temperature(middle) and OH mass fraction(bottom) for IEM mixing model with $C_\phi = 6$ at selected time.

amount of reaction. Later, this dark region also moves toward downstream to exit computational domain. Temperature contour plots and OH radicals contour plots are positively correlated since more reaction gives more heat release, which results in high temperature.

A specific time is chosen to show how different mixing models and mixing coefficients C_ϕ affect extinction gap. Fig. 5.3 shows cases with IEM mixing model. For cases with $C_\phi = 3$ and 4, no extinction gap is in sight since they are not burning, as discussed in section 4.3.1. For cases with $C_\phi = 5$, 6, 7 and 8, length of extinction gap decreases as C_ϕ increases. This relation of C_ϕ and extinction gap verifies again that C_ϕ positively relate to how much burning is present in the flame. Case with $C_\phi = 7$ shows two extinction gaps in a simulation, which may caused by changing of descending slope (strain rate) of pulsed function from large to small and back to large again. This phenomenon only happened in small amount of cases with appropriate mixing coefficient C_ϕ, which may due to that magnitude and variation of strain rate in this turbulent pulsed jet flame are not large enough when velocity of fuel tube is slowing down. However, this two gaps phenomenon are not clearly visible in experiment [16] and LES/PDF simulations [15].

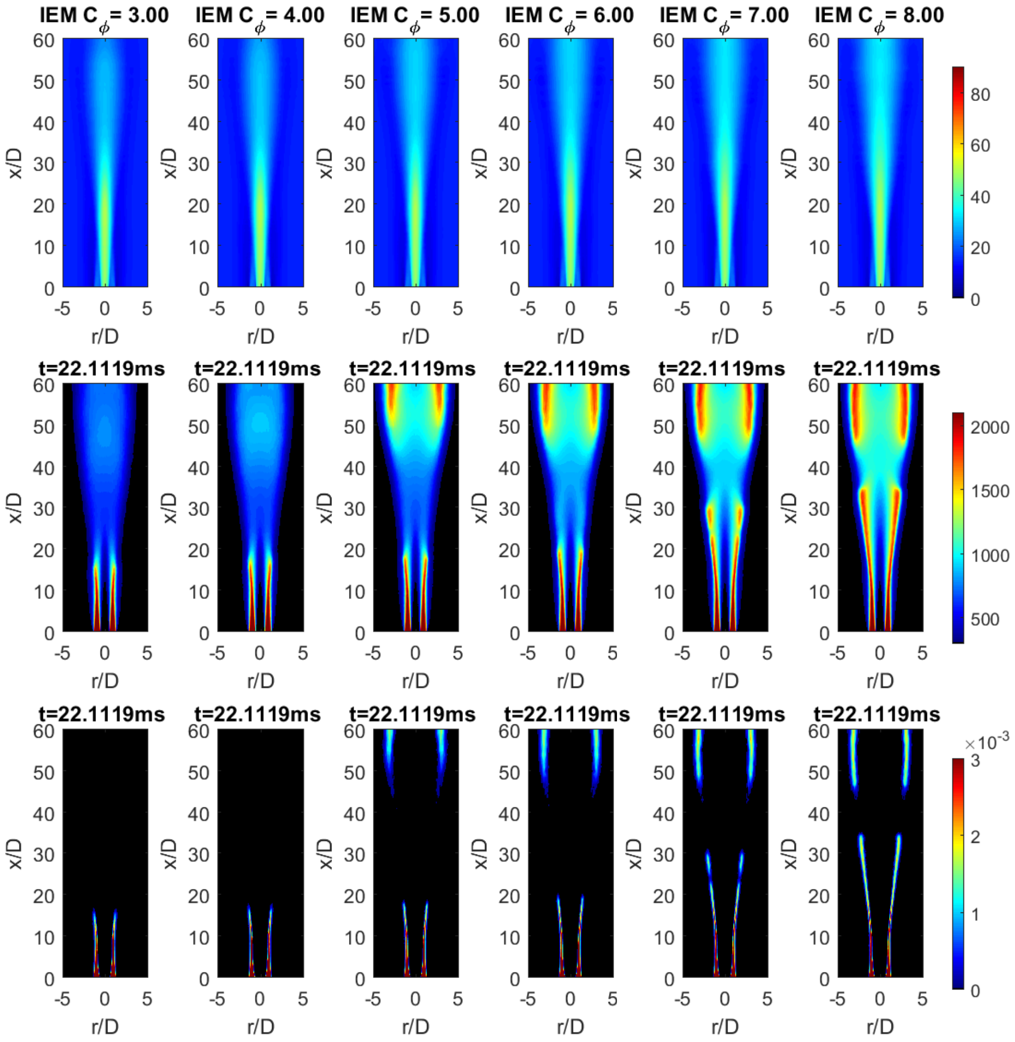

Figure 5.3. Contour plots for IEM model with different mixing coefficients C_ϕ at time t=22.1119ms. Mean axial velocity U (top), temperature (middle) and OH mass fraction (bottom) are presented.

Fig. 5.4 shows results from MCurl mixing model. Cases with mixing coefficient $C_\phi = 4$ and above showing as burning case and length of extinction gap decreases as C_ϕ increases. At $C_\phi = 8$, reaction is so strong that the OH radical reaction strips did not break during the whole pulse period.

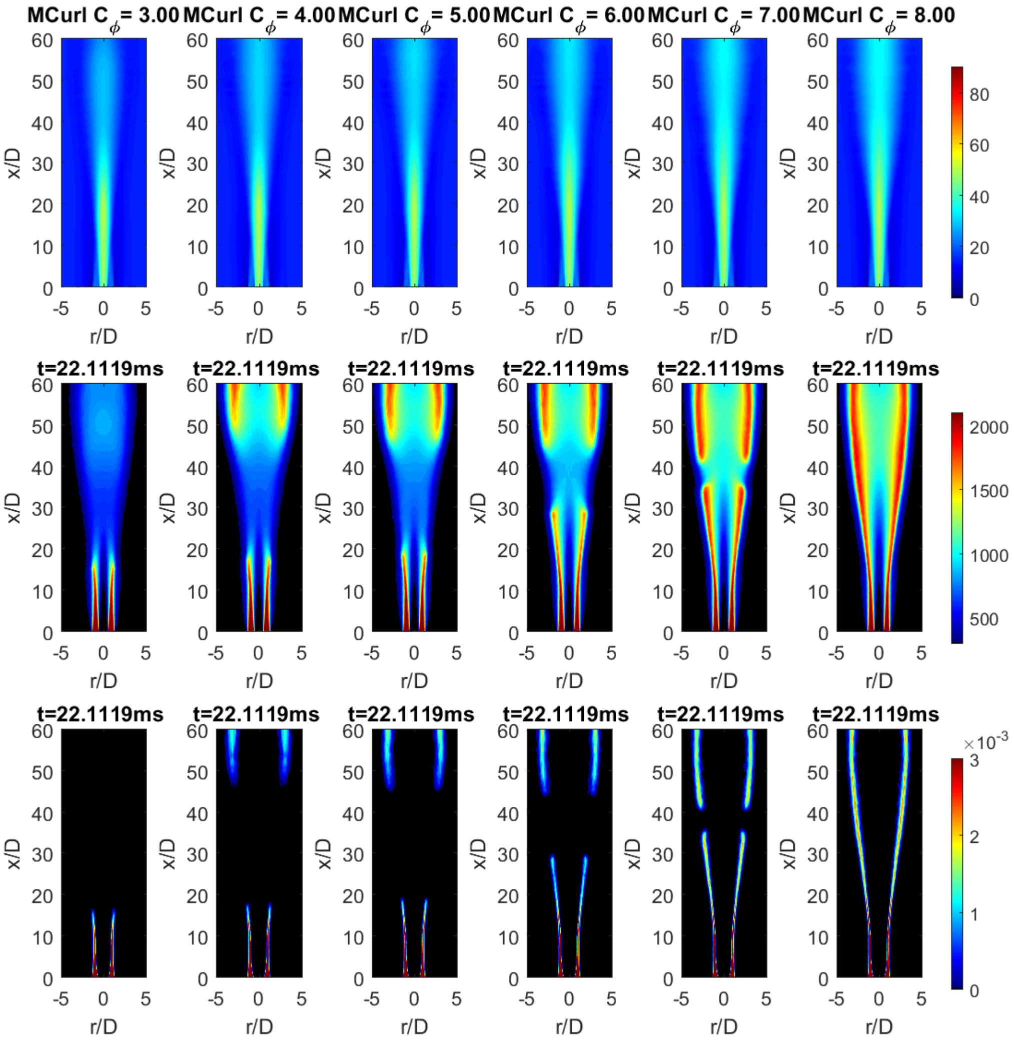

Figure 5.4. Contour plots for Modified Curl model with different mixing coefficients C_ϕ at time t=22.1119ms. Mean axial velocity U (top), temperature (middle) and OH mass fraction (bottom) are presented.

EMST results in fig. 5.5 are quite different from IEM and MCurl results. When decreasing mixing coefficient C_ϕ from normally used value $C_\phi = 2$, results does not show a trend to extinction. This does not like results with IEM and MCurl mixing model. However, it starts to show a spread out effect, which may related to EMST mining model's characteristic of localness.

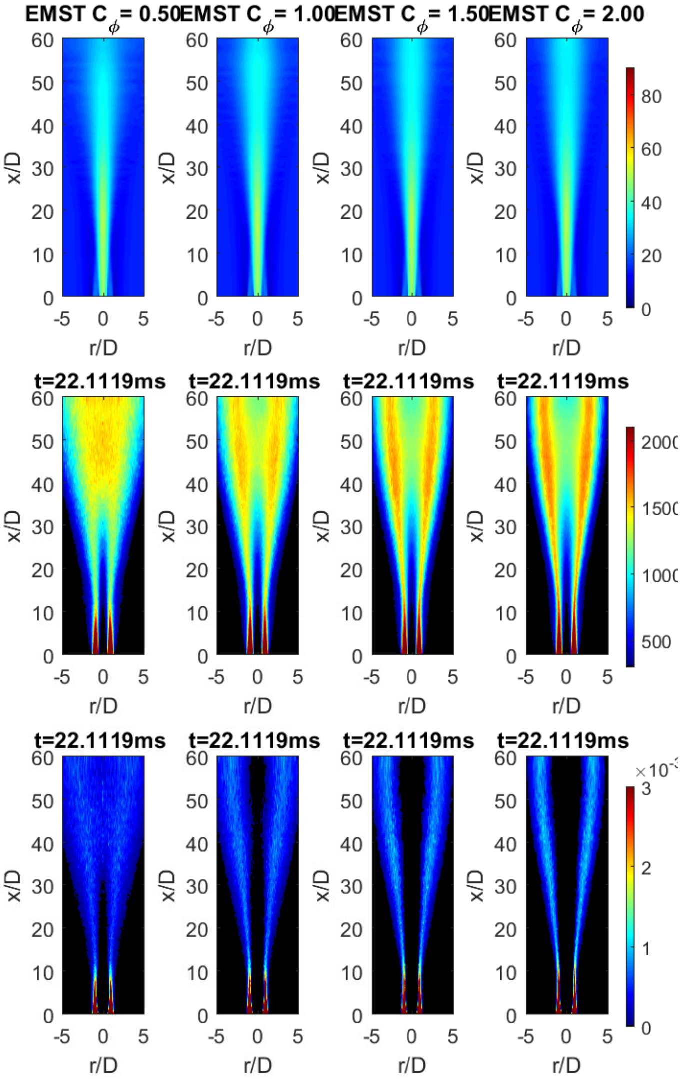

Figure 5.5. Contour plots for EMST model with different mixing coefficients C_ϕ at time t=22.1119ms. Mean axial velocity U (top), temperature (middle) and OH mass fraction (bottom) are presented.

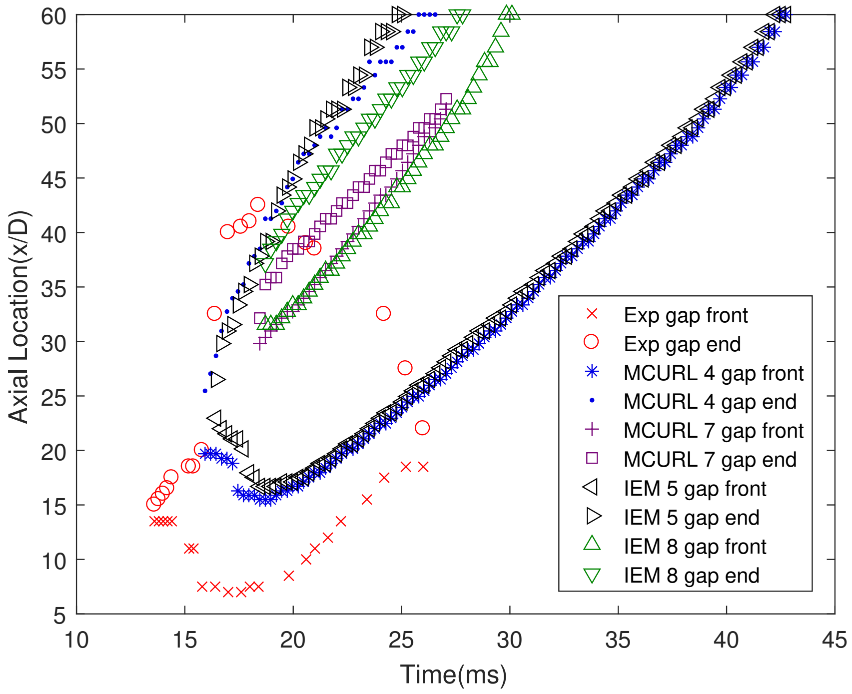

Figure 5.6. Extinction gap location time histories comparison between experimental data and simulation cases with IEM, MCurl mixing model.

Extinction gap location time histories are plotted in fig. 5.6. Gap location from experiment is acquired from the only OH radical video. Gap location from simulation result is generated by assuming following criteria for extinction: $T < 1200K$ and $Y_{\mathrm{OH}} < 5 \times 10^{-4}$. Although simulation results are quite different from experiment data, prediction of gap end during extinction are moving at a comparable speed when comparing to experimental data. Gap front also reveal a similar trend for $t < 25ms$ and cases with IEM $C_\phi = 5$ and MCurl $C_\phi = 4$.

5.2 Discussion and Comparison of Simulation Results

In this section, time history profiles comparison of experimental data and simulation results at selected locations are presented. Due to limitation of experimental data availability, only velocity data comparison is presented. Fig. 5.7-5.9 are radial profiles for IEM, MCurl and EMST mixing models.

Simulation result of U closely fits experimental data near burner exit for all three mixing models. Phase shifting of peak location is observed at axial location at$x/D =$ 10, 20 and 30 but not including $x/D = 50$ for all models. Since cases with EMST mixing model achieve high level of burning and does not form an extinction gap with small C_ϕ, huge over prediction of U during the extinction period is shown in fig. 5.8. IEM and MCurl mixing model also present a huge over prediction of U during extinction period with large C_ϕ. But for IEM mixing model with $C_\phi = 6$ and below, MCurl mixing model with $C_\phi = 5.5$ and below, velocity histories profiles show good agreement with experimental data.

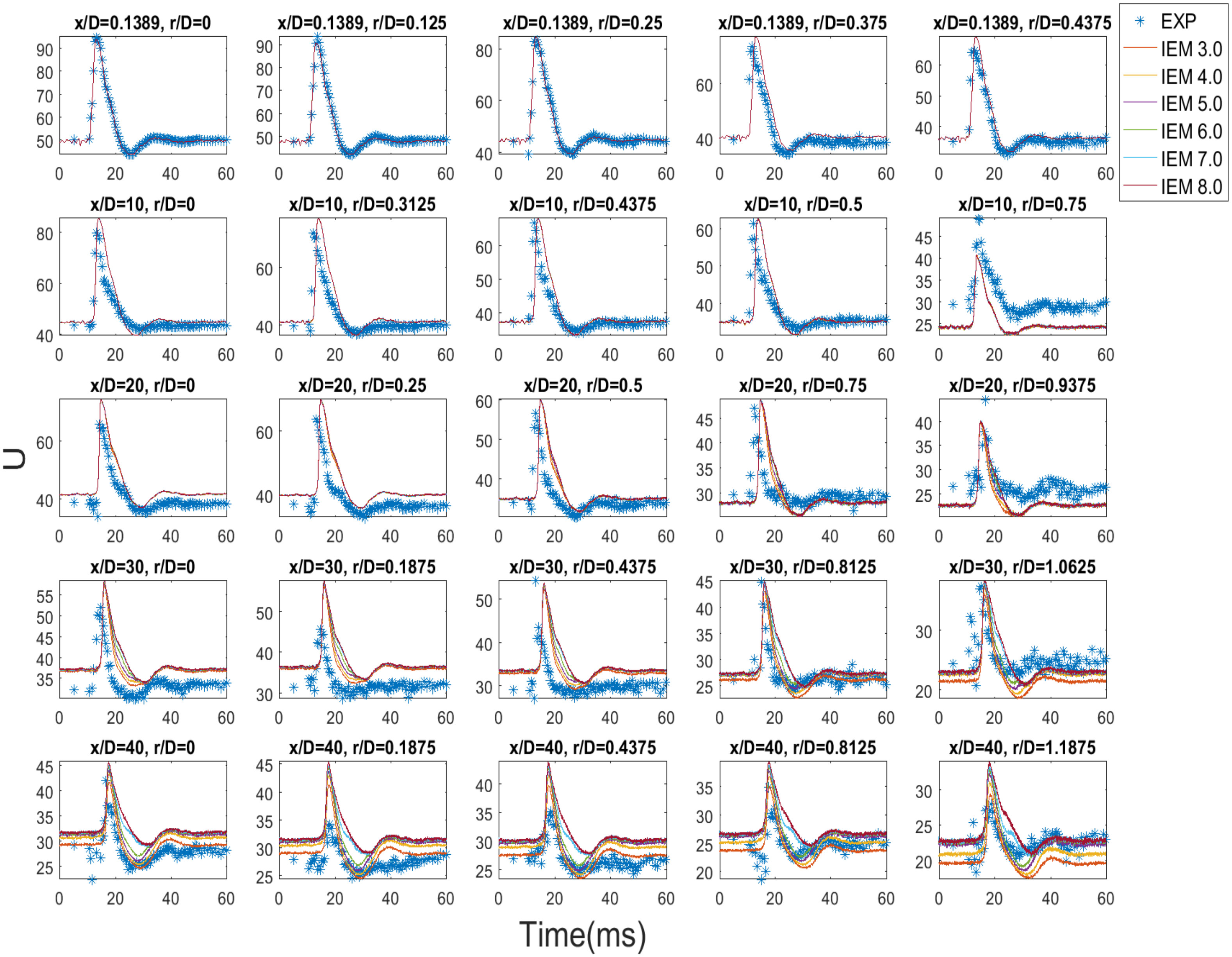

Figure 5.7. Time history of mean axial velocity U of experimental and cases with IEM mixing model at selected locations.

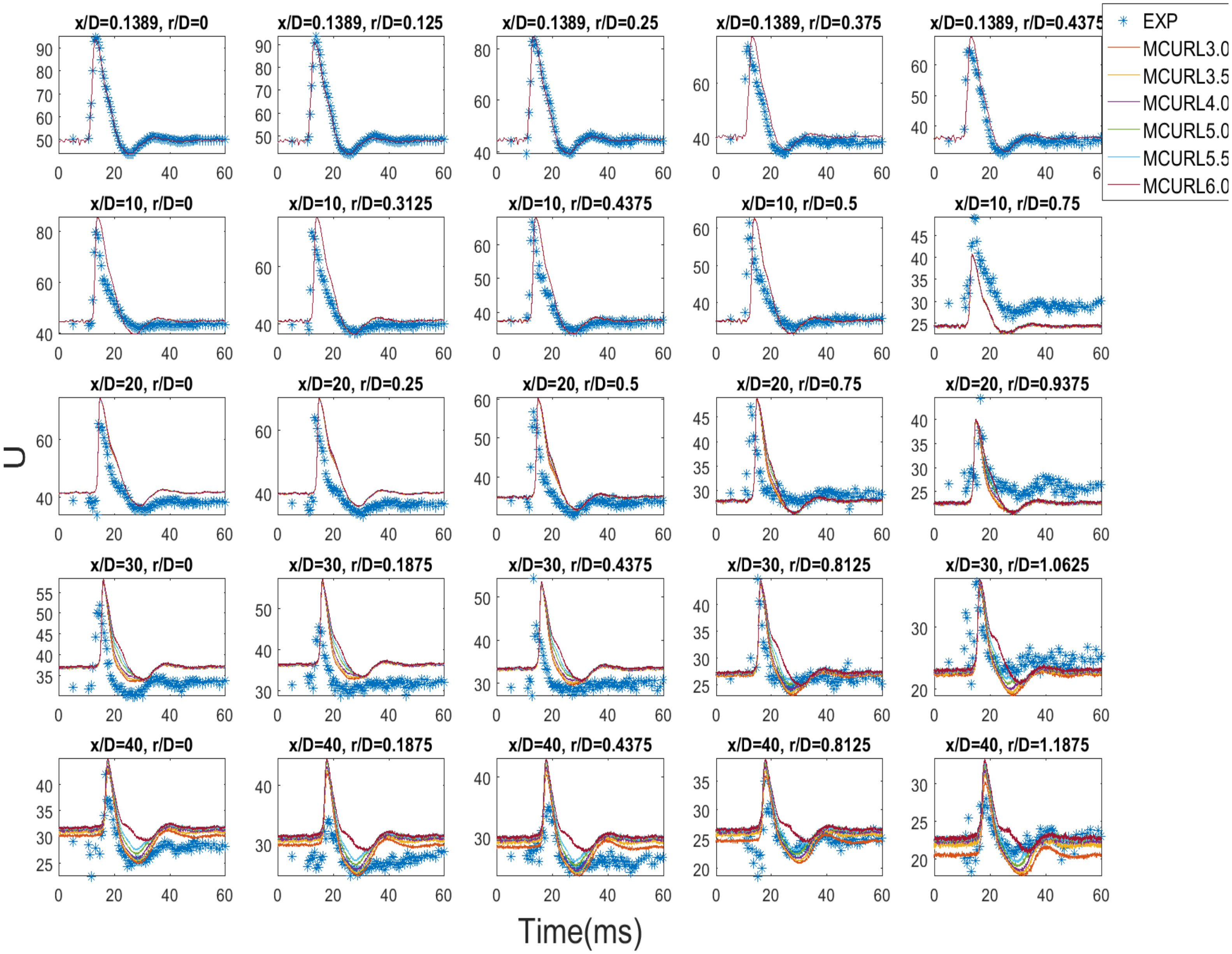

Figure 5.8. Time history of mean axial velocity U of experimental and cases with MCurl mixing model at selected locations.

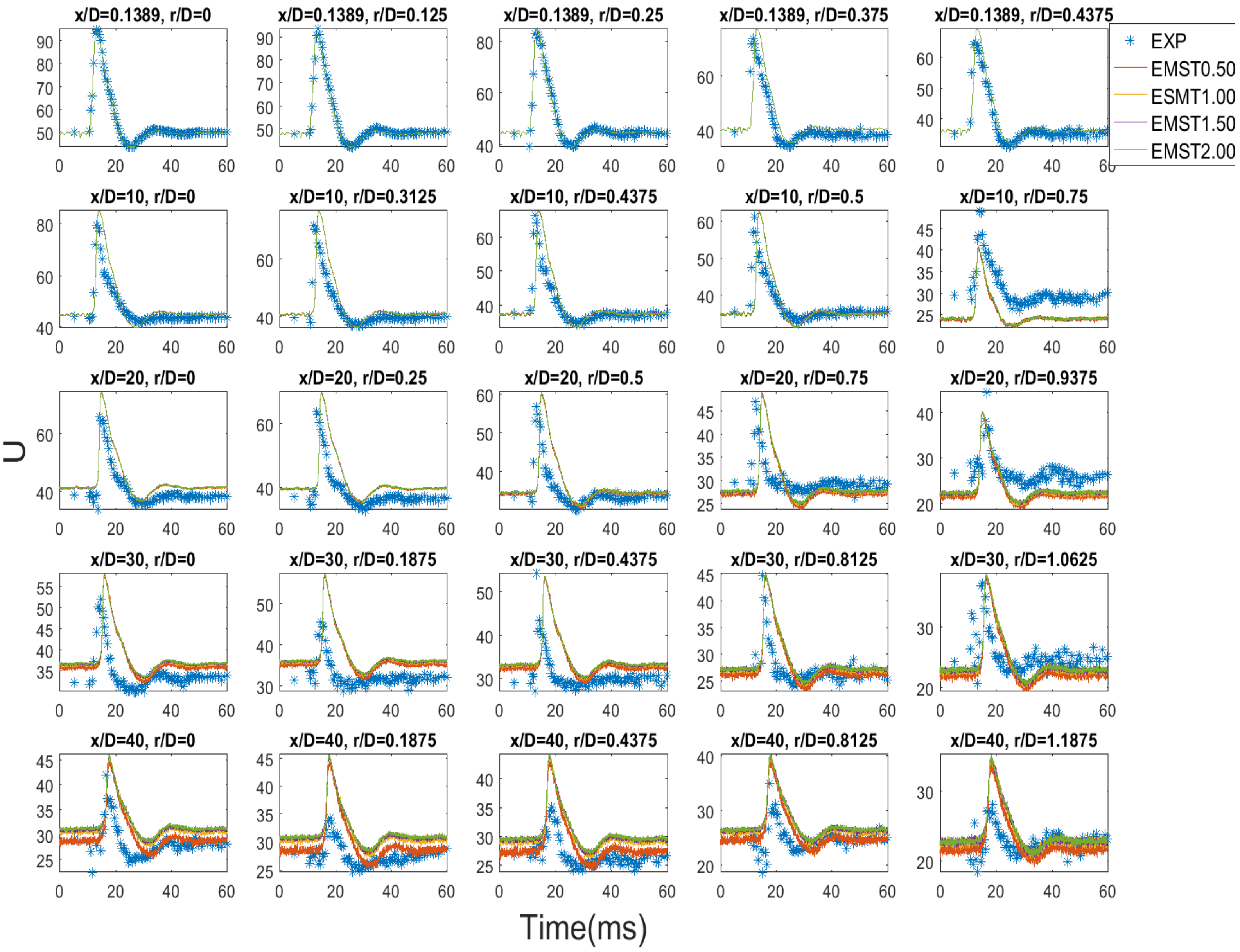

Figure 5.9. Time history of mean axial velocity U of experimental and cases with EMST mixing model at selected locations.

6. CONCLUSIONS

In this study, parametric studies are performed on the base flame of the turbulent pulsed jet flame, Flame L. Studies of effects of grid, $C_{\epsilon 1}$, Sc, mixing models, mixing coefficients and effective particle number are presented and an optimal simulation setting is acquired except for $C_{\epsilon 1}$, which a single value cannot match all experimental data. In the second half of this study, simulations of turbulent pulsed jet flame are calculated based on the optimal simulation setting obtained in parametric studies. Different mixing models and mixing coefficients are assessed in turbulent pulsed jet flame simulations. IEM and MCurl model are proved to have the capability to reproduce the extinction gap while EMST does not. Extinction gap is qualitatively studied and is observed that gap location and length varies with mixing models and mixing coefficients. Both IEM and MCurl model can capture similar extinction trend when compare to experimental data, but cannot capture the re-ignition correctly. Comparison of mean axial velocity between experimental data and simulation results is performed, good agreement between those two results is observed.

REFERENCES

REFERENCES

[1] Bp statistical review of world energy june 2017. https://www.bp.com/content/dam/bp/en/corporate/pdf/energy-economics/statistical-review-2017/bp-statistical-review-of-world-energy-2017-full-report.pdf.

[2] Tnf workshop abstract. http://www.sandia.gov/TNF/abstract.html.

[3] Steven A. Orszag and G.S. Patterson Jr. Numerical simulation of three-dimensional homogeneous isotropic turbulence. *Physical Review Letters*, 28(2):76–79, 1972.

[4] Douglas G. Fox and Douglas K. Lilly. Numerical simulation of turbulent flows. *Reviews of Geophysics and Space Physics*, 10(1):51–72, 1972.

[5] J. Smagorinsky. General circulation experiments with the primitive equations. *Monthly Weather Review*, 91(3):99–164, 1963.

[6] B. E. Launder and B. I. Sharma. Application of the Energy-Dissipation Model of Turbulence to the Calculation of Flow near a Spinning Disc. *Letters in Heat and Mass Transfer*, 1(2):131–137, 1974.

[7] *Turbulence Modeling for CFD.* DCW Industries, Inc., 2006.

[8] S.B. Pope. Pdf methods for turbulent reactive flows. *Progress in Energy and Combustion Science*, 11:119–192, 1985.

[9] Burner image of sydney piloted flame. http://web.aeromech.usyd.edu.au/thermo-fluids/images/pilote2.jpg.

[10] A.R. Masri, R.W. Bilger, and R.W. Dibble. Turbulent nonpremixed flames of methane near extinction: Mean structure from raman measurements. *Combustion and Flame*, 71:245–266, 1988.

[11] S.H. Starner and R.W. Bilger. Characteristics of a piloted diffusion flame designed for study of combustion turbulence interactions. *Combustion and Flame*, 61:29–38, 1985.

[12] R.W. Dibble, A.R. Masri, and R.W. Bilger. The spontaneous raman scattering technique applied to nonpremixed flames of methane. *Combustion and Flame*, 67:189–206, 1987.

[13] A.R. Masri. PhD thesis, University of Sydney, 1987.

[14] Haifeng Wang, Mrinal Juddoo, Sten H. Starner, Assaad R. Masri, and Stephen B. Pope. A novel transient turbulent jet flame for studying turbulent combustion. *Proceedings of the Combustion Institute*, 34:1251–1259, 2012.

[15] Assaad R. Masri Pei Zhang and Haifeng Wang. Studies of the flow and turbulence fields in a turbulent pulsed jet flame using les/pdf. *Combustion Theory and Modelling*, 21:897–924, 2017.

[16] Assaad Masri Mrinal Juddoo, Agisilaos Kourmatzis. An experimental study of transient effects in a pulsed, piloted, nonpremixed turbulent jet flame. In *9th Asia-Pacific Conference on Combustion*, 2013.

[17] W.P. Jones and B.E. Launder. The prediction of laminarization with a two-equation model of turbulence. *International Journal of Heat and Mass Transfer*, 15:301–314, 1972.

[18] A. Kazakov and M. Frenklach. Reduced reaction set based on gri-mech 1.2. `http://combustion.berkeley.edu/drm/`.

[19] S.B. Pope. Computationally efficient implementation of combustion chemistry using in situ adaptive tabulation. *Combustion Theory and Modelling*, 1:41–63, 1997.

[20] Habib N. Najm Michael A. Singer, Stephen B. Pope. Modeling unsteady reacting flow with operator splitting and isat. *Combustion Theory and Modelling*, 147:150–162, 2006.

[21] Zhuyin Ren Liuyan Lu, Steven R. Lantz and Stephen B. Pope. Computationally efficient implementation of combustion chemistry in parallel pdf calculations. *Cornnel University report FDA*, 02, 2007.

[22] J. Villermaux and J.C. Devillon. Interaction by exchange with the mean. In *Second International Symposium On Chemical Reaction Engineering*, 1972.

[23] W.Kolbe J. anicka and W. Kollmann. Closure of the transport equation for the probability density function of turbulent scalar fields. *Journal of Non-Equilibrium Thermodynamics*, 4:47–66, 1979.

[24] S. Subramaniam and S. B. Pope. A mixing model for turbulent reactive flows based on euclidean minimum spanning trees. *Combustion And Flame*, 115:487–514, 1998.

[25] Kukjin Kim Haifeng Wang. Effect of molecular transport on pdf modeling of turbulent non-premixed flames. *Proceeding of the Combustion Institute*, 35:1137–1145, 2015.

[26] S.B. Pope. Pdf/monte carlo methods for turbulent combustion and their implementation on parallel computers. *Turbulence and Molecular Processes in Combustion*, pages 51–62, 1993.

[27] R.L. Curl. Dispersed phase mixing: I. theory and effects of simple reactors. *AIChEJ*, 9:175–181, 196.

[28] P.A. Nooren, H.A. Wouters, T.W.J. Peeters, D. Roekaerts, U. Maas, and D. Schmidt. Dispersed phase mixing: I. theory and effects of simple reactors. *Combust. Theory Modelling*, 1:79–96, 1997.

[29] Haifeng Wang and Stephen B. Pope. Large eddy simulation/probability density function modeling of a turbulent jet flame. *Proceedins of the Combustion Institue*, 33(1):1319–1330, 2011.

[30] Haifeng Wang and Stephen B. Pope. Time-averaging strategies in the finite-volume/particle hybrid algorithm for the joint pdf equation of turbulent reactive flows. *Combustion Theory and Modelling*, 12(3):529–544, 2008.